

Locality of topological dynamics in Chern insulators.

A. A. Markov^{1, 3*}, D. B. Golovanova^{1, 2}, A. R. Yavorsky^{1, 2}, and A. N. Rubtsov^{1, 3}

¹Russian Quantum Center, Moscow 121205, Russia

²Moscow Institute of Physics and Technology, Dolgoprudny, 141701, Russia

³Lomonosov Moscow State University, Moscow 119991, Russia

*markov.anton92@gmail.com

ABSTRACT

A system having macroscopic patches in different topological phases have no well-defined global topological invariant. To treat such a case, the quantities labeling different areas of the sample according to their topological state are used, dubbed local topological markers. Here we study their dynamics. We concentrate on two quantities, namely local Chern marker and on-site charge induced by an applied magnetic field. We demonstrate that the time-dependent local Chern marker is much more non-local object than equilibrium one. Surprisingly, in large samples driven out of equilibrium, it leads to a simple description of the local Chern marker's dynamics by a local continuity equation. Also, we argue that the connection between the local Chern marker and magnetic-field induced charge known in static holds out of equilibrium in some experimentally relevant systems as well. This gives a clear physical description of the marker's evolution and provides a simple recipe for experimental estimation of the topological marker's value.

1 Introduction

A defining property of topological insulators is the formation of robust conducting modes between patches with different topological indices^{1,2}. This property has many potential applications such as dissipationless power lines³, new generations of inductors⁴ and other electronic devices⁵, as well as quantum computation⁶. Therefore, the ability to detect topologically homogeneous patches inside a sample and control their position is of both fundamental and practical interest.

Topologically inhomogeneous samples require special care from a theoretical perspective. Global topological indices, e.g. Chern number⁷, are not applicable directly to such systems, as they characterise the whole system. Recently, a family of quasi-topological quantities, called local topological markers, has been developed and studied⁸⁻¹¹. In equilibrium, such markers depend on the exponentially localized density matrix's elements. Thus, one uses local information to estimate a global topological index. Topological markers are not necessarily strictly quantized; rather the average of the marker over large areas of a system tends towards a quantised value¹². The requirement that a marker is a local representative of a global index does not produce a unique definition. Indeed, the Chern number has several local counterparts^{8-11,13}, each coming with its own merits and drawbacks.

It is very tempting to use local markers to understand the evolution of the topological properties of a system out of equilibrium. Every marker has its own "natural" time-dependency. This raises the question, what physical information the time-dependence of markers contain and whether it is the same information for different markers. Also, for dynamical systems there are additional requirements for a quantity to be considered well-behaved. Perhaps most importantly, one expects that a local quantity would have local dynamics. That is, the evolution of a local quantity should obey a local continuity equation. In gapped systems one might also hope that the information needed to calculate the value of a marker is local. In equilibrium this condition follows^{12,14} from the exponential decay of correlations with distance¹⁵.

Several intriguing properties of time-dependent topological markers have been found¹⁶⁻¹⁹. Local topological markers in finite systems can change^{18,19}, unlike the global Chern number, which is unaffected by unitary evolution^{16,20}. Previous work has conjectured¹⁹ that the dynamics of the local Chern marker⁹ are governed by local currents emanating from the system's boundaries, defined implicitly through the lattice continuity equation on the marker.

In the present manuscript we discuss the locality of the markers' dynamics and the physical information contained in them for free fermionic systems out of equilibrium. We concentrate on two quantities, the local Chern marker⁹ and the localized version of the Streda formula^{21,22}. We demonstrate that in general, nonequilibrium markers are highly non-local quantities, in contrast to the equilibrium case. That is, the calculations require knowledge of the density matrix elements $\langle \hat{c}^\dagger(\mathbf{r})\hat{c}(\mathbf{0}) \rangle$ at large distances $|\mathbf{r}| \gg 1$ in units of the lattice spacing. Paradoxically, we will see that this non-locality leads directly in large finite samples to a local continuity equation for the local Chern marker. Also, we argue that the equilibrium connection between the local Chern number and the Streda-like on-site response holds under dynamics in some experimentally relevant systems. The manuscript continues our earlier preprint²³.

The manuscript is organized as follows. In Section 2 we introduce the systems that we study and the local topological markers suitable for them. In Section 3 we define their counterparts out of equilibrium and discuss the localization properties of their dynamics. Thereafter, the limits when the connection between the local Chern marker and local Streda formula holds are considered. In Section 4 we numerically test our observations in quench dynamics. In Section 5 we numerically study the possibility to change the position of phase boundaries in a finite 2D Chern insulator. For a start, we studied an almost adiabatic case. We conclude with a discussion of possible directions for the further research and possible experimental verification of our results.

2 Chern insulators and their local topological markers

We consider non-interacting lattice fermions in two spatial dimensions. In the absence of symmetries other than $U(1)$, topological phases of such systems are classified by the Chern number $C^{7,24}$. Physically, it corresponds to the Hall conductivity of the system. We suppose that the Hamiltonian has the following form:

$$\hat{H} = \sum_{\mathbf{r}_1, \mathbf{r}_2} H^{ss'}(\mathbf{r}_1, \mathbf{r}_2) \hat{c}_s^\dagger(\mathbf{r}_1) \hat{c}_{s'}(\mathbf{r}_2) + h.c., \quad (1)$$

where the index s stands for on-site degrees of freedom, e.g. spin and orbital. We assume exponential decay of the Hamiltonian's matrix elements with distance. In an insulating phase this leads to exponentially decaying density matrices^{15,25}.

Strictly speaking, topological phases with $C \neq 0^7$ are realized in the thermodynamic limit on a torus. Real-world samples subjected to open boundary conditions necessarily contain topological boundaries. Furthermore, a sample may contain macroscopically large patches in different phases. Local topological markers allow us to label different parts of the system according to their ‘‘Chern number’’ in such settings^{8–11}.

Topological markers come in different forms and have been suggested based on different lines of thought about the physics of Chern insulators. Let us briefly review the main types and the physical intuition behind them. Kitaev's marker⁸ was proposed as a bulk estimation of the energy flow at the edges of a system – the chiral central charge. The Bott index¹⁰ physically originated as an obstruction for Wannier orbitals to be exponentially localized. The local Chern marker^{9,26} was proposed as a local real space estimation of the Chern number. Finally, local response functions^{13,22} can be used to extract the information about the Hall conductivity, and thus amount to a topological index.

In the following we concentrate our attention on the two local markers: the Local Chern Marker (LCM) and a local version of the Streda formula for the Hall conductivity²¹.

Local Chern Marker can be considered as a localized form of a generalization of the Chern number suitable for systems without a notion of momentum space, as appeared for the first time in Ref.²⁷:

$$C(\mathbf{r}) = -2\pi i \text{Tr} \left(\hat{\delta}_{\mathbf{r}} \hat{P} \hat{X} \hat{P} \hat{Y} \hat{P} \right) + c.c. = \text{Tr} \left(\hat{\delta}_{\mathbf{r}} \hat{C} \right). \quad (2)$$

where $\hat{\delta}_{\mathbf{r}} = \sum_s |\mathbf{r}_s\rangle \langle \mathbf{r}_s|$ is the single-particle projection to a site at the position \mathbf{r} , with s labelling any on-site degrees of freedom, $\hat{P} = \sum_{i \in occ} |\psi_i\rangle \langle \psi_i|$ is the projector to the occupied single-particle states. \hat{X} and \hat{Y} are the position operators. We use the notation \hat{C} for the Chern marker operator $\hat{C} = -2\pi i \hat{P} \hat{X} \hat{P} \hat{Y} \hat{P} + h.c.$ The locality of the marker results from the exponential localization of the projector $\hat{P}(\mathbf{r}, \mathbf{r}')$ in gapped systems²⁵.

Local Streda Marker. The LCM can be connected to localized Hall response. Explicitly the connection was demonstrated in Ref.¹³ for a local cross-conductivity. Less rigorously, a thermodynamical argument was used^{11,12} to connect the LCM to the response in the form of a localized Streda formula. Throughout the manuscript we will call it the local Streda marker:

$$C_S(\mathbf{r}) = \phi_0 \frac{\delta n(\mathbf{r})}{\delta \phi} = \phi_0 \text{Tr} \left(\hat{\delta}_{\mathbf{r}} \frac{\delta \hat{P}}{\delta \phi} \right). \quad (3)$$

Here, the variation of the average on-site density $n(\mathbf{r})$ is taken with respect to a uniform magnetic field B_z perpendicular to the sample, with a flux ϕ through a unit cell. The field is supposed to be turned on adiabatically. Throughout the paper we will measure magnetic flux in units of the flux quanta $\phi_0 = \frac{2\pi\hbar}{e}$.

In Appendix A we demonstrate that the two markers coincide in the equilibrium at least in two limits. First, along the same lines as in Ref.²⁸ we prove the equivalence for spectrally flat two-band Hamiltonians. Second, we prove it for translationally invariant patches of systems with a symmetric spectrum.

For the following discussion we would also need explicit corrections to the projectors linear in ϕ . In Appendix A, we demonstrate, that in the two discussed limits the corrections are:

$$\frac{\delta \hat{P}}{\delta \phi} = \pi i (\hat{Q} \hat{X} \hat{P} \hat{Y} \hat{P} + \hat{P} \hat{X} \hat{P} \hat{Y} \hat{Q}) + h.c. = -2\pi i \hat{P} \hat{X} \hat{P} \hat{Y} \hat{P} + \pi i (\hat{X} \hat{P} \hat{Y} \hat{P} + \hat{P} \hat{X} \hat{P} \hat{Y}) + h.c.. \quad (4)$$

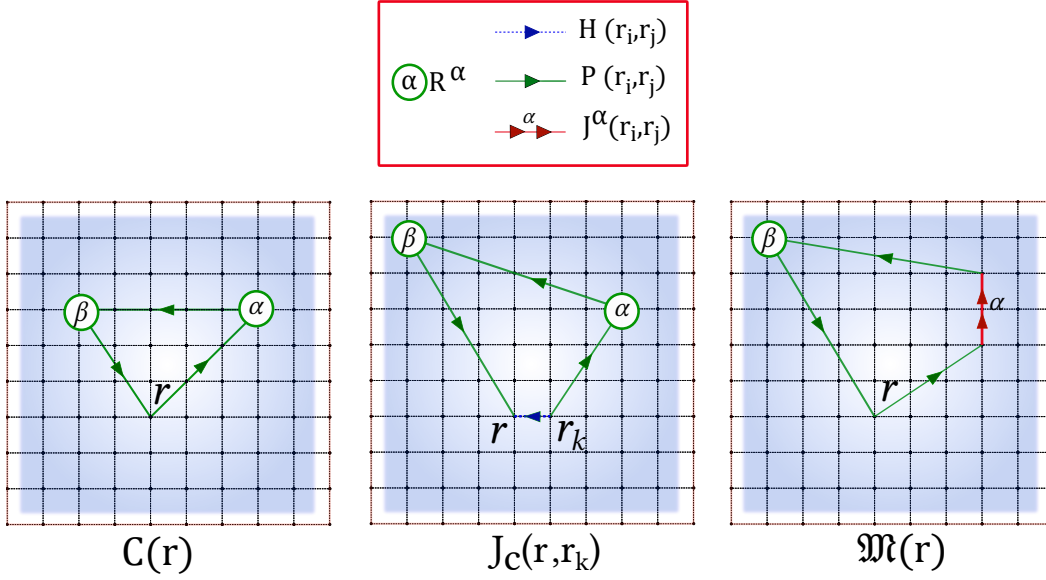


Figure 1. Real-space diagrams corresponding to the LCM $C(\mathbf{r})$ (2) and the two contributions $J_c(\mathbf{r})$ and $\mathfrak{M}(\mathbf{r})$ to its time-derivative, see Eq. (6). All the quantities are the sums of terms represented by all possible polygons in the figure. Each green line on the diagram corresponds to a multiplication by the density matrix element connecting two sites. A circle with a greek letter in it, corresponds to multiplication by x or y component of a site position \mathbf{r} . Distinct letters imply distinct components. The blue line represents the Hamiltonian matrix elements between a pair of sites. The red line represents matrix elements of the current operator $\hat{J}^\alpha = -i[\hat{H}, \hat{R}^\alpha]$

Let us note that in general the Streda marker and Local Chern marker do not coincide even in equilibrium. For instance, while in the presence of weak diagonal disorder their values are very close to each other¹¹, however once disorder is introduced in the hopping amplitude, the discrepancy between the two becomes quite noticeable, see Appendix A.

3 Topological markers' dynamics

3.1 Local Chern Marker

An appealing approach to define LCM out of equilibrium is to use the same function of the projector onto filled states as in Eq. (2) and allow the projector to evolve^{16–19}:

$$C(\mathbf{r}, t) = -2\pi i \text{Tr} \left(\hat{\delta}_r \hat{P}(t) \hat{X} \hat{P}(t) \hat{Y} \hat{P}(t) \right) + c.c., \quad (5)$$

Thus defined, the local Chern marker is guaranteed to give correct topological information if a steady-state is reached with well defined topological properties.

Previous works on the dynamics of topological markers^{16,17,19} have revealed several important features. First, in finite systems the average of such topological markers can change in contrast to global topological indices^{16,18,20}. Importantly, their evolution reflects the change in a topological phase^{16,17,19}. Second, it was conjectured, based on the simulations that the dynamics of the LCM is governed by local currents¹⁹.

The equations of motion for the Chern operator \hat{C} are not the Heisenberg ones because \hat{C} depends on an instantaneous state of a system. Therefore, the operator evolves even in the Schrodinger picture. Explicitly the time derivative of the marker can be expressed as:

$$\begin{aligned} \dot{C}(\mathbf{r}, t) &= -2\pi \text{Tr} \left(\hat{\delta}_r [\hat{H}, \hat{P}] \hat{X} \hat{P} \hat{Y} \hat{P} + \hat{P} \hat{X} [\hat{H}, \hat{P}] \hat{Y} \hat{P} + \hat{P} \hat{X} \hat{P} \hat{Y} [\hat{H}, \hat{P}] \right) + c.c. \\ &= -2\pi \text{Tr} \left(\hat{\delta}_r [\hat{H}, \hat{P} \hat{X} \hat{P} \hat{Y} \hat{P}] - \hat{P} [\hat{H}, \hat{X}] \hat{P} \hat{Y} \hat{P} - \hat{P} \hat{X} \hat{P} [\hat{H}, \hat{Y}] \hat{P} \right) + c.c. \\ &= \sum_{\mathbf{r}_i} J_c(\mathbf{r}, \mathbf{r}_i) + \mathfrak{M}(\mathbf{r}). \end{aligned} \quad (6)$$

Here in the last line we have separated two contributions. The usual Heisenberg-like term $J_c(\mathbf{r})$:

$$J_c(\mathbf{r}, t) = i \text{Tr} (\hat{\delta}_r [\hat{H}(t), \hat{C}(t)]), \quad (7)$$

describes the current of the marker to neighboring sites. The remaining part in the r.h.s. of Eq. 6, denoted as

$$\mathfrak{M}(\mathbf{r}, t) = 2\pi \text{Tr} \left(\hat{\delta}_r \hat{P} [\hat{H}, \hat{X}] \hat{P} \hat{Y} \hat{P} + \hat{\delta}_r \hat{P} \hat{X} \hat{P} [\hat{H}, \hat{Y}] \hat{P} \right) + c.c., \quad (8)$$

describes ‘‘teleportation’’ of the marker values from a given site to all sites it is correlated with, as we shall see in Section 4.3 and in more detail in Appendix D. This teleportation is local only when the projectors are localized. That is, if the matrix elements of \hat{P} in the position basis satisfy $P(\mathbf{r}, \mathbf{r}_1) \approx 0$ for $|\mathbf{r} - \mathbf{r}_1| \gg 1$. For out-of-equilibrium dynamics the long-range correlations are also important. Surprisingly, in the presence of long-range correlations the equations of motions are almost exactly local.

Dynamics of the Chern marker are dominated by the J_c term whenever the correlations are spread across the sample. That is, when the \mathbf{r} matrix elements of the instantaneous projector \hat{P} in the position basis are non-zero at large separations: $P(\mathbf{r}, \mathbf{r}_1) \neq 0$ for $|\mathbf{r} - \mathbf{r}_1| \approx N$, where N is the system size. Then the following holds:

$$\frac{J_c(\mathbf{r})}{\mathfrak{M}(\mathbf{r})} \sim N \quad (9)$$

This can be seen most clearly from the real-space diagrams, corresponding to the terms shown in Fig.1. These are drawn to represent the trace in definitions 7 and 8 as a sum in the position basis. Both $J_c(\mathbf{r})$ and $\mathfrak{M}(\mathbf{r})$ can be represented as a sum of all possible quadrangles with the sides representing the matrix elements of \hat{P} and \hat{H} . In the two vertices a contribution to the current term $J_c(\mathbf{r})$ is multiplied by the x and y coordinates of a point. In the case of long-range correlations, these coordinates can be of the order of the systems’ size N . On the other hand, the $\mathfrak{M}(\mathbf{r})$ term is multiplied by a coordinate of order N only once, as one of the coordinate operators is commuted with the Hamiltonian. Thus, the $H(\mathbf{r}_1, \mathbf{r}_2)(\mathbf{r}_1^\alpha - \mathbf{r}_2^\alpha)$ is of order unity, where \mathbf{r}^α stands for x or y component of the vector \mathbf{r} . Therefore Eq. (9) holds, provided that the largest contribution to $J_c(\mathbf{r})$ and $\mathfrak{M}(\mathbf{r})$ are due to the terms corresponding to the long-ranged diagrams.

When $J_c(\mathbf{r}) \gg \mathfrak{M}$ for all times, the Chern marker always satisfies the lattice continuity equation and the Chern marker can be approximated by

$$C(\mathbf{r}, t) \approx \text{Tr} \left(\hat{\delta}_r \hat{U}(t) \hat{\mathfrak{C}}(0) \hat{U}^\dagger(t) \right) \equiv \mathfrak{C}(\mathbf{r}, t). \quad (10)$$

Here $\mathfrak{C}(0)$ is the Chern marker operator at the initial moment $t = 0$. Note the von Neumann-like ordering of the evolution operators $\hat{U}(t)$ around the operator $\mathfrak{C}(0)$.

Eq. (10) can be used for estimation of LCM for all the times of evolution in large translationally invariant patches. In the thermodynamic limit on torus bulk marker can not change^{16,20}. Evolution of the marker in such systems always starts at the boundaries and then penetrates the bulk at the Lieb-Robinson²⁹ velocity v_{LR} . Therefore, in the bulk, the marker starts to evolve only when long-range correlations with the edges are built.

3.2 Local Streda Formula

One could use the same approach as with the local Chern marker to define the local Streda marker out of equilibrium. That would result in Eq. (4) with the projectors P substituted with the time-dependent ones $P(t)$. This way the equivalence between local Chern marker and local Streda marker would hold in the two discussed limits. However, from experimental point of view this approach requires ability to freeze the evolution of $P(t)$ at the moment t and then adiabatically slow turning on uniform magnetic field. This is hardly achievable in real experiment.

In a real experiment, one would rather apply magnetic field to an initial state and when allow the system to undergo dynamics. From this perspective, time dependent C_S should be defined as:

$$C_S(\mathbf{r}, t) = \frac{\delta n(\mathbf{r}, t)}{\delta \phi} = \text{Tr} \left(\delta_r \frac{\delta \hat{P}(t)}{\delta \phi} \right), \quad (11)$$

where we have assumed that at $t = -\infty$ the magnetic field was adiabatically turned on. Thus, at $t = 0$ the system is initialized in the ground state of the system with a vanishingly small uniform magnetic field B_z perpendicular to the sample with a flux ϕ through each unit cell. Importantly we require that no magnetic field is present during the evolution. Otherwise local Streda marker does not behave well at late times of order $t \approx \frac{2N}{v_{LR}}$, see the discussion in Appendix B.

Let us stress that $C_S(\mathbf{r}, t)$ does not guarantee to convey the correct information about a steady-state’s topological properties. However in some cases the correspondence between $C_S(\mathbf{r}, t)$ and $C(\mathbf{r}, t)$ can be established.

Suppose that at time $t = 0$ a system is prepared in the ground state of Hamiltonian such that the conditions for the formula Eq. (4) are met. Therefore we can express the evolution of the correction to the projector, to first order in B , as:

$$\frac{\delta \hat{P}(t)}{\delta \phi} = \hat{U}(t) \hat{\mathfrak{C}}(0) \hat{U}^\dagger(t) + \pi i \hat{U}(t) (\hat{X} \hat{P} \hat{Y} \hat{P} + \hat{P} \hat{X} \hat{P} \hat{Y} - h.c.) \hat{U}^\dagger(t). \quad (12)$$

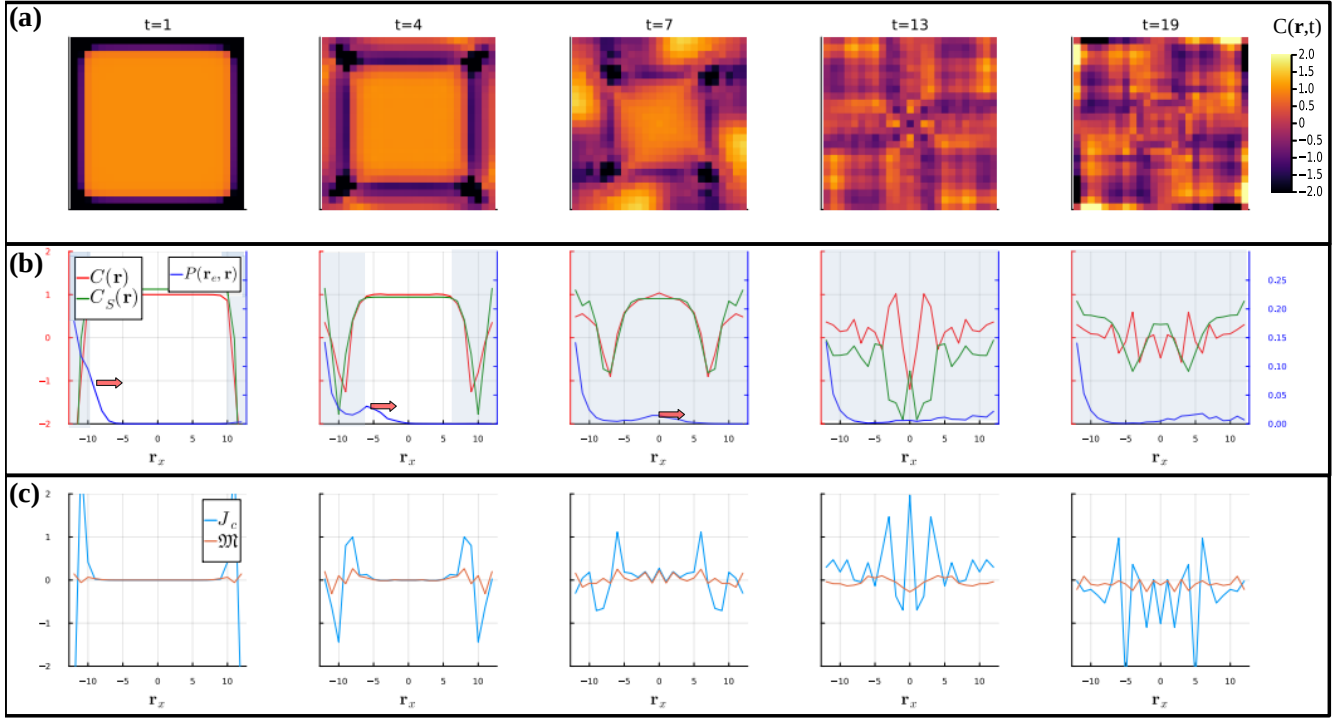


Figure 2. Quench dynamics in the QWZ model. (a) Distribution of the LCM (5) over a 25x25 sample at different times. (b) Distribution of the LCM $C(\mathbf{r}, t)$, local Streda marker $C_S(\mathbf{r}, t)$ (11) and the norm of matrix elements $|P(\mathbf{r}_e, \mathbf{r}, t)|$ along the middle $y = 0$ slice of the system. The site r_e is chosen at the left edge. Right (blue) y-axis is for the projector matrix elements $|P(\mathbf{r}_e, \mathbf{r}, t)|$; left (red) y-axis is for the markers' distributions. The red arrows points direction of the maximum of the correlation propagation front. The blue shadows mark the area there markers has already started to evolve. (c) Distributions of $J_c(\mathbf{r}, t)$ (7) and $\mathfrak{M}(\mathbf{r}, t)$ (8) along the middle $y = 0$ slice of the system at different times.

If only the first term is taken into account, one come to an approximation:

$$C_S(\mathbf{r}, t) \approx \text{Tr} \left(\hat{\delta}_r \hat{U}(t) \hat{C}(0) \hat{U}^\dagger(t) \right) \approx C(\mathbf{r}, t). \quad (13)$$

The other terms in Eq. (11) give no contribution to the marker in the equilibrium, see Appendix A. In time-dependent case, they are responsible for deviations of the local Streda marker from both $C(\mathbf{r}, t)$ and $\mathfrak{C}(\mathbf{r}, t)$. Numerically we have found that for the times $C(\mathbf{r}, t)$ and $\mathfrak{C}(\mathbf{r}, t)$ are different, these additional terms put the local Streda marker between the two, making $C_S(\mathbf{r}, t)$ even a better estimation for a time-dependent local Chern marker.

The locality of the Streda marker evolution is evident. Indeed, the markers' evolution can be described in terms of a local continuity equation by comparing the evolution of two systems. One that evolving in a probing magnetic field and another that evolves without it:

$$\begin{aligned} \dot{C}_S(\mathbf{r}, t) &= -\partial_t \frac{\delta n(\mathbf{r}, t)}{\delta \phi} = -i \frac{\delta [H, n(\mathbf{r})]}{\delta \phi} = -\frac{\delta (\sum_{r_1, s, s'} H^{s, s'}(\mathbf{r}, \mathbf{r}_1) \hat{c}_s^\dagger(\mathbf{r}) \hat{c}_{s'}(\mathbf{r}_1) + h.c.)}{\delta \phi} = -\frac{\delta \sum_{r_1} J^e(\mathbf{r}, \mathbf{r}_1)}{\delta \phi} \\ & \dot{C}_S(\mathbf{r}, t) = -\text{div} \mathbf{J}_S^e(\mathbf{r}, t). \end{aligned} \quad (14)$$

Here we have denoted the variation of electric current w.r.t. probe magnetic field as the Streda marker current: $\mathbf{J}_S^e(\mathbf{r}, \mathbf{r}', t) = -\frac{\delta \mathbf{J}^e(\mathbf{r}, \mathbf{r}', t)}{\delta \phi}$. Eq. 11 forces the markers' dynamics to be local.

Therefore, one can think about the currents of the local Streda Marker in terms of the real electron currents caused by a uniform probe magnetic field.

4 Quench Dynamics

In this section we discuss the markers' evolution after a sudden change of parameters in concrete models. We shall see three different regimes of the markers' dynamics. First, we discuss examples of quench dynamics in a sample with a translationally

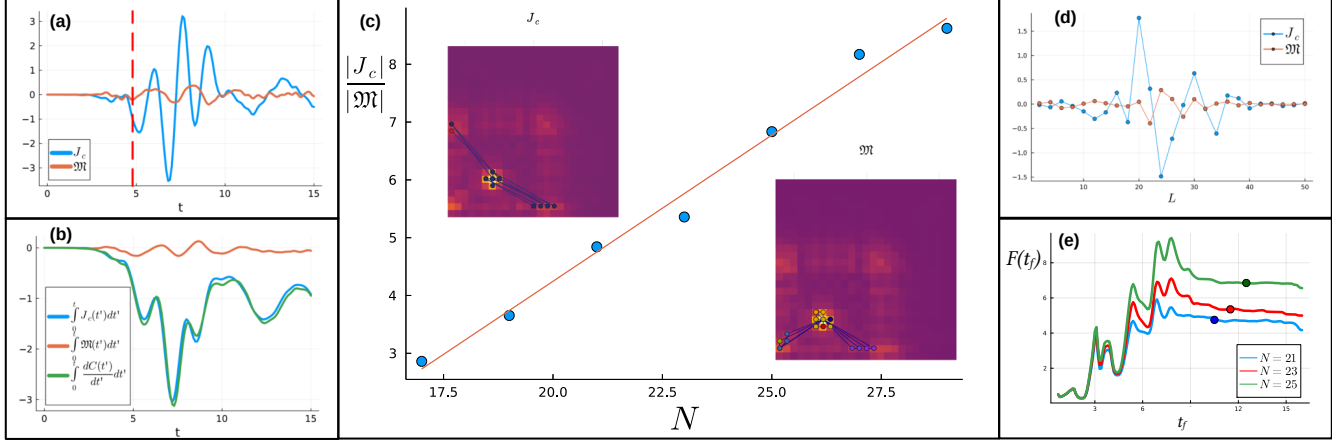


Figure 3. Quench dynamics in QWZ. (a) Time evolution of $J_c(\mathbf{r}_b)$ and $\mathfrak{M}(\mathbf{r}_b)$ (6) at a fixed site $\mathbf{r}_b = (-7, -6)$ in the bulk of a 25×25 sample. Vertical red line marks the moment $t_f = 5$ when both $J_c(\mathbf{r}_b, t)$ and $\mathfrak{M}(\mathbf{r}_b, t)$ have their first pronounced extrema. (b) Time evolution of the LCM $C(\mathbf{r}_b, t)$ at \mathbf{r}_b and integral contribution to the local Chern marker $C(\mathbf{r}_b, t)$ from $J_c(\mathbf{r}_b, t)$ and $\mathfrak{M}(\mathbf{r}_b, t)$ (c) The square root of the ratio of spectral powers of $J_c(\mathbf{r}_b, t)$ and $\mathfrak{M}(\mathbf{r}_b, t)$ (see Eq. (18)), as a function of the system's linear size N . Insets demonstrate the ten most contributing real-space diagrams as in Fig. 1 for $J_c(\mathbf{r}_b, t_f)$ and $\mathfrak{M}(\mathbf{r}_b, t_f)$. The diagrams are plotted above the distribution $|P(\mathbf{r}_b, \mathbf{r})|$. (d) The contribution of diagrams of the length L to the $J_c(\mathbf{r}_b, t_f)$ and $\mathfrak{M}(\mathbf{r}_b, t_f)$. L is defined as perimeter of each polygon in Fig. 1 in the Manhattan metric. (e) The square root of the ratio of spectral powers of $J_c(\mathbf{r}_b, t)$ and $\mathfrak{M}(\mathbf{r}_b, t)$ F (see Eq. (18)) as a function of the upper limit t_f of the integration over time.

invariant bulk. Here, J_c prevails over \mathfrak{M} over the whole evolution. Therefore, the Streda marker and local Chern marker should be approximately equal to each other. Next, we consider quench dynamics in the Hofstadter-Harper model^{30,31}. In this case, the translation invariance of the bulk bulk is formally broken. As we shall see, it is enough to allow the marker to evolve in the bulk from the very start. Thus, at early times \mathfrak{M} and J_c are comparable. As we shall see, it results in a larger discrepancy between the Streda and Chern markers. Finally we will present an example of the opposite limit, $\mathfrak{M} \gg J_c$. In this case the Chern and Streda marker are very different.

4.1 Translationally Invariant Bulk. QWZ model.

We use a Chern insulator model introduced in Ref. ³² by Qi, Wu and Zhang (QWZ) to illustrate the case of a translationally invariant bulk. It is a two-band particle-hole symmetric model, thus its spectrum is symmetric with respect to the Fermi level. Therefore, Eq. (4) applies to the case. The QWZ Hamiltonian is given by

$$\hat{H}_{QWZ} = \sum_{\mathbf{r}} t_h (\hat{c}_s^\dagger(\mathbf{r}) \frac{\sigma_z - i\sigma_x}{2} \hat{c}_{s'}(\mathbf{r} + \mathbf{e}_x) + \hat{c}_s^\dagger(\mathbf{r}) \frac{\sigma_z - i\sigma_y}{2} \hat{c}_{s'}(\mathbf{r} + \mathbf{e}_y) + h.c.) + \sum_{\mathbf{r}} m(\mathbf{r}, t) \hat{c}_s^\dagger(\mathbf{r}) \sigma_z \hat{c}_{s'}(\mathbf{r}), \quad (15)$$

where the Pauli matrices σ_i act on the spin subspace indexed by s , \mathbf{e}_x and \mathbf{e}_y are the unit vectors to the neighboring sites of a square lattice, t_h is the hopping parameter, which we set to one.

In the translationally invariant case where $m(\mathbf{r})$ is constant, the Chern number is determined by the parameter m ⁱ:

$$\begin{aligned} -2 < m < 0 & \text{ topological; } C = 1 \\ 0 < m < 2 & \text{ topological; } C = -1 \\ m < -2, m/ > 2 & \text{ trivial; } C = 0 \end{aligned} \quad (16)$$

Let us consider a finite system subject to open boundary conditions initialized in the ground state of the Hamiltonian H_0 with m equal to -1 . This corresponds to a topological phase with $C = 1$. Then at $t = 0$, m suddenly changes its value to -3 , corresponding to a trivial Hamiltonian H_1 . Thus:

$$\hat{U}(t) = \exp(-i\hat{H}_1 t) \quad (17)$$

ⁱNote, that the model appears in the literature in different flavours. Also, topological indices used, may differ in sign. We hold to the conventions of the book³³, so that the topological index and the Hall conductivity have the same sign

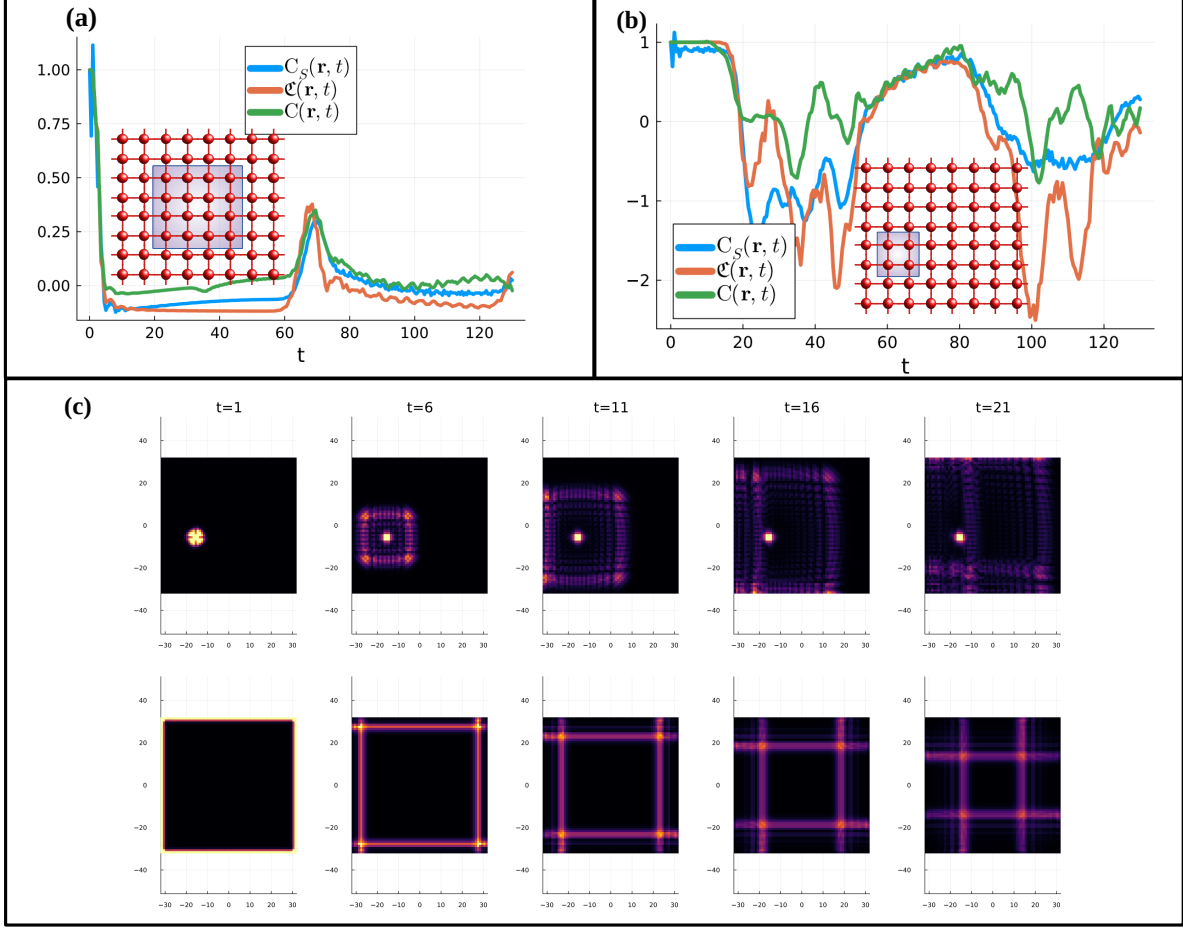


Figure 4. Correspondence between C_S and C . Time dependencies $C_S(\mathbf{r}, t)$, $C(\mathbf{r}, t)$ and $\mathfrak{C}(\mathbf{r}, t)$, Eq. (13) averaged over different number of bulk sites of a 64×64 sample. The insets demonstrates schematically the sites over which the markers are averaged. $C_S(\mathbf{r}, t)$ was calculated as a numerical derivative of the density with respect to an external probe magnetic field. (a) The markers are averaged over almost all the bulk sites, the indent from the boundary is equal to two sites. (b) The average is taken over a small 5×5 region, with the coordinates $(-15, -5)$ of the left bottom corner. (c) Top row shows propagation of correlations between the site $(-15, -5)$ and all the others. Bottom row demonstrates the propagation of the density from the edge states to the bulk.

The edges are characterized by long-range correlations and thus J_c is larger than \mathfrak{M} due to the larger contribution from the long ranged diagrams. As time progresses, the points at the edges become correlated with the points at the bulk. Therefore, the value of the marker starts to evolve also in the bulk. The spread of the LCM currents to the bulk is presented in Fig. 2. The top row shows the distribution of the local Chern marker over a finite sample at different times.

The speed of the markers' currents front propagation is determined by the speed of propagation of the correlations. This is illustrated in the middle row of Fig. 2, where we present the distribution of the LCM $C(\mathbf{r})$ along the middle y -section of the sample and the norm of projector elements $P(\mathbf{r}_e, \mathbf{r})$ between site at the left boundary \mathbf{r}_e and all other sites in the slice. One can see that speed at which the correlator front propagates through the system is identical to the speed of the marker currents. Two points become correlated when they could have exchanged information. For non-interacting particles, the fastest way to convey information is to produce an entangled particle-hole pair in the middle between the two sites. Then the particle should propagate to one of the sites, while the hole to the other³⁴. Therefore, the Lieb-Robinson velocity and the speed of the LCM's current propagation is $v_{LR} = v_h^{max} + v_p^{max}$, in correspondence with the fitting of Ref.¹⁹.

Let us now inspect more closely the suggestion that

$$\frac{J_c(\mathbf{r})}{\mathfrak{M}(\mathbf{r})} \sim N. \quad (9)$$

Both $J_c(\mathbf{r}_b)$ and $\mathfrak{M}(\mathbf{r}_b)$ oscillate and reach zero at some moments. Therefore we should rather characterize the ratio of the amplitudes of their oscillations. We investigated the ratio of their spectral power: $P = \int_0^\infty d\omega |J_c(\mathbf{r}_b, \omega)|^2 / |\mathfrak{M}(\mathbf{r}_b, \omega)|^2$. Here $J_c(\mathbf{r}_b, \omega)$ and $\mathfrak{M}(\mathbf{r}_b, \omega)$ are Fourier transforms of $J_c(\mathbf{r}_b)$ and $\mathfrak{M}(\mathbf{r}_b)$. According to Parseval's theorem it is equal to the time integrated ratio of their modulus squared: $P = \int_0^\infty dt' |J_c(\mathbf{r}_b, t')|^2 / |\mathfrak{M}(\mathbf{r}_b, t')|^2$. This quantity should be quadratic in N according to Eq. (9). Therefore, we take a square root of the spectral power to obtain a quantity linear in N :

$$F = \sqrt{\int_0^{t_f} \frac{|J_c(\mathbf{r}_b, t')|^2}{|\mathfrak{M}(\mathbf{r}_b, t')|^2} dt'}, \quad (18)$$

at a fixed site \mathbf{r}_b in the bulk. The time t_f is chosen such that the correlations are spread across the whole system. In our units the speed of correlation propagation is $v_{LR} \approx 2$. Therefore, we took $t_f = N/2$. As can be seen in Fig. 3(e), the ratio Eq. (18) reaches a plateau close to t_f .

F depends on the number of sites N linearly to a very good approximation, as demonstrated in Fig. 3c. This can be attributed to the contribution from the long ranged diagrams in Fig. 1. Both $J_c(\mathbf{r})$ and $\mathfrak{M}(\mathbf{r})$ get the largest contribution from such diagrams, as illustrated in Fig. 3e, where the contribution to $J_c(\mathbf{r}_b)$ and $\mathfrak{M}(\mathbf{r}_b)$ from the diagrams of length L is plotted at time $t = 5$, when $J_c(\mathbf{r}_b)$ and $\mathfrak{M}(\mathbf{r}_b)$ are reaching their first pronounced maximum. Also, the ten diagrams giving the largest contribution are shown in the insets of Fig. 3c. These diagrams are plotted on top of the $|P(\mathbf{r}_b, \mathbf{r})|$ distribution. We can see that the typical diagrams contributing the most are these, connecting the site \mathbf{r}_b to the front of the correlations' spread.

Given that $J_c \gg \mathfrak{M}$ for all times, we might expect that the approximation (13) should work. The correspondence between $C_S(\mathbf{r}, t)$ and $C(\mathbf{r}, t)$ is illustrated in the middle row of Fig. 2 and in Fig. 4. At some moments the difference between $C_S(\mathbf{r}, t)$ and $C(\mathbf{r}, t)$ is noticeable as we can see at the times from around $t = 13$ till $t = 19$ in Fig. 2 and at the times around $t = 20$ in Fig. 4. At these times correlation front is being reflected from the border and passes the site or the area, as can be seen in top row of Fig. 4(c). Therefore, at these times local correlations become more important. From the perspective of the local Streda marker, the times of deviation correspond to the edge states density propagating through the site or area we are interested in, see bottom row of Fig. 4(c). However, when the average over all bulk sites is taken, the approximation (13) works better, see Fig. 4. Remarkably, it holds for very long times. In fact we have not found upper bound limitations in time for Eq. (13).

4.2 Hofstadter-Harper model

Now, let us examine how the situation changes in the absence of translational symmetry in the bulk. The conceptually simplest way to destroy it is to add an on-site disorder to the bulk. We consider this case in Appendix C. Here, we discuss a more subtle example of a formal translation symmetry breaking. We discuss a quench across a topological phase transition in the Harper-Hofstadter model^{30,31,36}. It describes a single-band of electrons on a square lattice in the presence of the uniform magnetic field. The Hamiltonian reads:

$$H_{hh} = - \sum_{\langle i,j \rangle, s} (t_{ij} c(\mathbf{r}_i)_s^\dagger c(\mathbf{r}_j)_s + h.c.). \quad (19)$$

The magnetic field is coupled to the system using Peierl's substitution³⁷, which introduces a site-dependent phase factor in the hopping matrix t_{ij}

$$t_{ij} = t_h \cdot e^{i \frac{2\pi}{\phi_0} \int_{\mathbf{r}_i}^{\mathbf{r}_j} \mathbf{A}(\mathbf{r}) \cdot d\mathbf{r}}. \quad (20)$$

Here, t_{ij} denotes the hopping amplitude between neighboring sites at position \mathbf{r}_i and \mathbf{r}_j . The spectrum of the Hamiltonian is the famous Hofstadter butterfly presented in Fig. 5(a). We study quenches from the uniform magnetic field with a flux $\phi = 1/3\phi_0$ through a unit cell to one with $\phi = 1/6\phi_0$, at a fixed chemical potential $\mu = -1/3 t_h$. This corresponds to quench from $C = 1$ three band system to a $C = 2$ six-band model, see Fig. 5(a).

In the symmetric gauge, the vector potential of a uniform magnetic field is given by $\mathbf{A}(\mathbf{r}) = \frac{1}{2} B(-y, x, 0)$. Here, both the initial and post-quench Hamiltonian cannot be diagonalized in momentum space. Therefore, the preservation of the Chern number is not guaranteed by the arguments in Refs^{16,20}. As we shall see, in this case the evolution starts in the bulk as well as at the boundaries. This is rather counter-intuitive, as the Hamiltonian can be diagonalized in momentum space when one is working in the Landau gauge, provided that ϕ equals a rational multiple of the magnetic flux quantum ϕ_0 (i.e., $\phi = \frac{p}{q} \phi_0$). Therefore it might be tempting to conclude that the Chern marker can change its value only at the boundaries. That is indeed what would happen if we were working in the Landau gauge. In fact, the two situations are not gauge equivalent. At the very moment of quench (at $t = 0$) they differ by a very large electric field applied to the system, see Ref.³⁸ for the details. Therefore the density evolution in the two situations differs significantly.

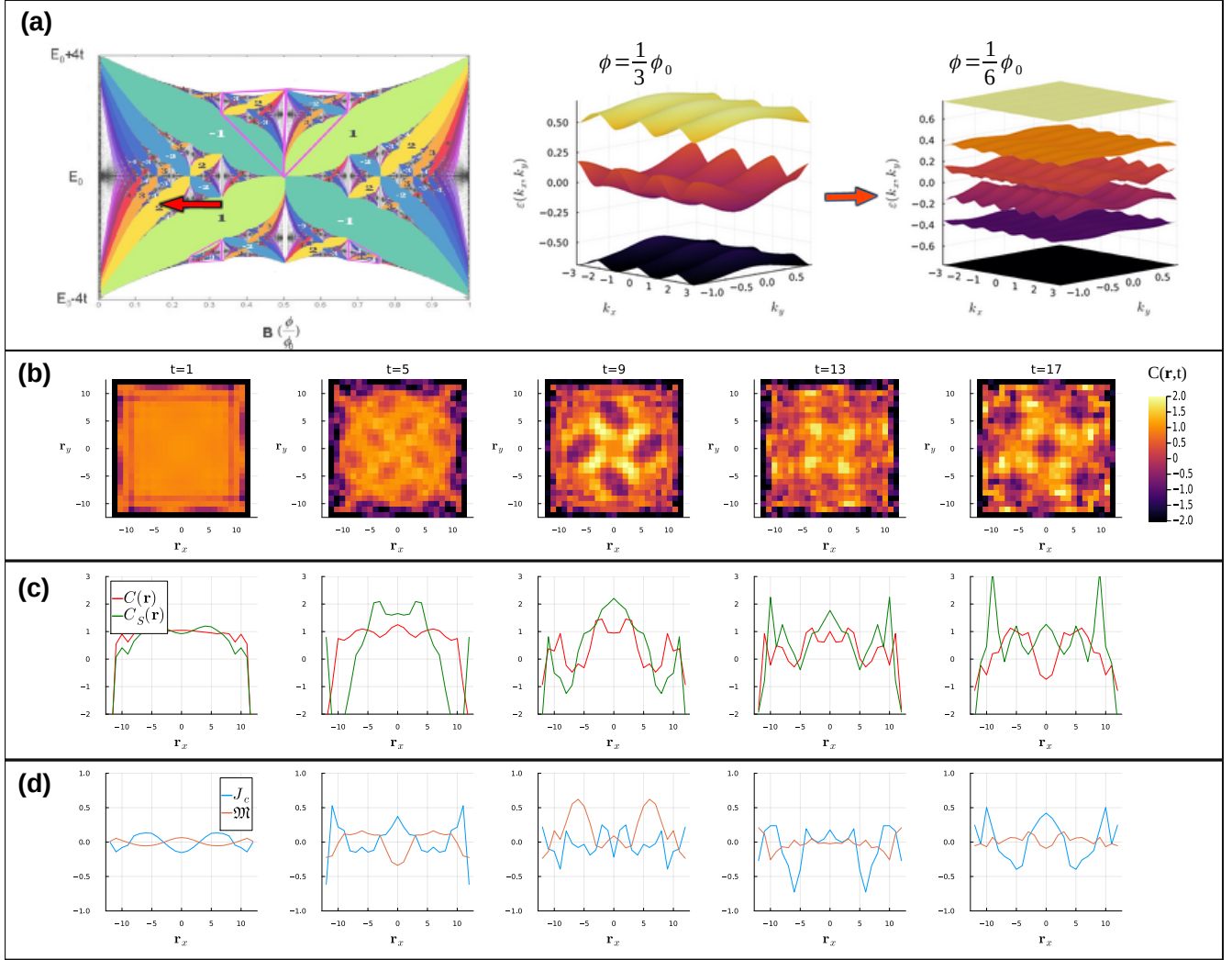


Figure 5. Quench dynamics of Harper-Hofstadter model. (a) The spectrum of the Hofstadter-Harper model³¹ shown against the strength of uniform magnetic field and at particular values $\phi = 1/3\phi_0$ and $\phi = 1/6\phi_0$. The arrows marks the initial $\phi = 1/3\phi_0$ and post-quench $\phi = 1/6\phi_0$ values of the field. The Hofstadter's butterfly is readopted from Ref.³⁵ (b) Distribution of the LCM over a 25×25 sample at different times. (c) Distribution of the LCM $C(\mathbf{r}, t)$ and $C_S(\mathbf{r}, t)$ along the middle - $y = 0$ slice of the system. (d) Distributions of the $J_c(\mathbf{r})$ and $\mathfrak{M}(\mathbf{r})$ along the middle - $y = 0$ slice of the system at different times.

Several differences w.r.t. to the QWZ model are noticeable. First, the evolution of the LCM no longer starts at the edges, marker currents are present throughout bulk, see Fig. 5(b). Therefore, at short times there is no guarantee that $J_c(\mathbf{r}, t) \gg \mathfrak{M}(\mathbf{r})$. In fact, as can be seen in Fig. 5(d), for some regions $\mathfrak{M}(\mathbf{r})$ exceeds $J_c(\mathbf{r}, t)$. The difference in $C(\mathbf{r}, t)$ and $C_S(\mathbf{r}, t)$ is more pronounced than in the QWZ model. However, some resemblance can be still observed. This suggests that the correspondence between $C(\mathbf{r}, t)$ and $C_S(\mathbf{r}, t)$ might hold more generally then in the discussed limits of symmetric or flat spectra, although some averaging procedure might be necessary.

4.3 Non-local transport of the marker.

The currents described by the \mathfrak{M} term cannot be localized to neighboring sites. Most clearly, it can be observed in the following exaggerated example. The scheme is shown in Fig. 6(a). Consider a translationally invariant sample in the topological phase. At time $t = 0$ a central site is cut off from the rest of the system. That is, all the hoppings to and from the site are quenched to zero. Simultaneously, the on-site parameters are changed. If $C(\mathbf{r}, t)$ were to satisfy a lattice continuity equation, no change of the marker would be observed on that site, however as can be seen in Fig. 6(b), the on-site value of the marker does change.

J_c measures the distance in terms of the instantaneous Hamiltonian. That is $J_c = i[\hat{H}(t), \hat{C}(t)]$ is non-zero is only for the two sites i and j connected by the hopping term $\hat{H}(\mathbf{r}_1, \mathbf{r}_2)$ and J_c decays at least as fast as the Hamiltonian does. Therefore, in the

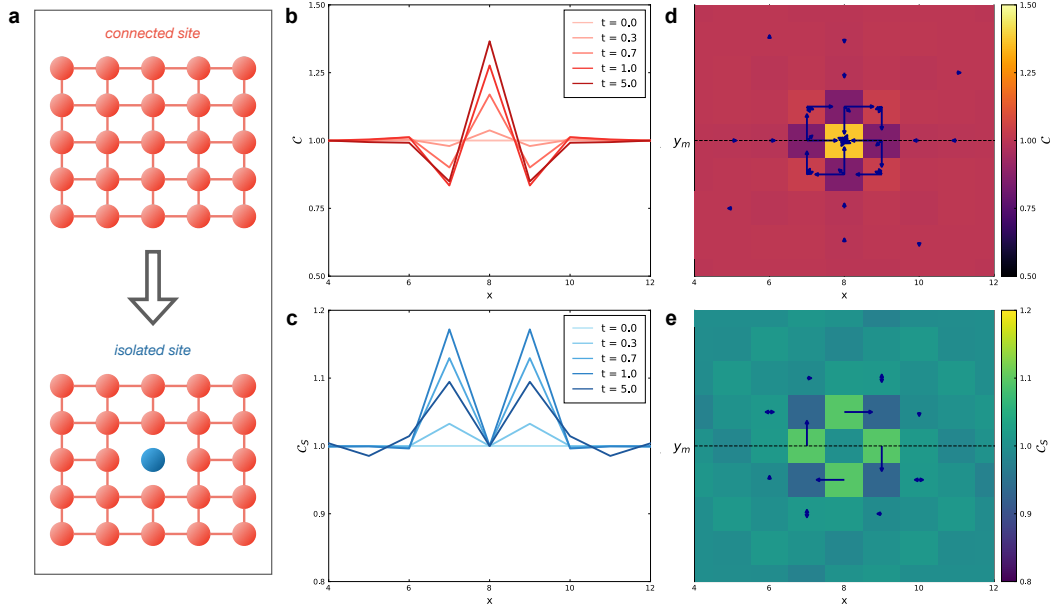


Figure 6. The dynamics of the LCM under quench isolating a single site in the sample’s middle. **a** The scheme of the "cutt-off" scenario. At the $t=0$ the hoppings from the central site are set to zero. Simultaneously the on-site parameters are changed. **b-c** LCM $C(\mathbf{r},t)$ (5) and the local Streda marker $C_S(\mathbf{r},t)$ (11) at the middle section of the system at different moments of time. **d-e** The color map shows the distributions of the markers. Blue arrows show topological marker currents defined in Appendix D for LCM and in Eq. (14) for the local Streda marker.

setting depicted in Fig. 6(a), J_c vanishes at the central cite, as the hopping parameters from it are set to zero. Therefore, in this particular case the evolution is governed solely by \mathfrak{M} .

The term \mathfrak{M} depends on the instantaneous Hamiltonian in a subtle way. \mathfrak{M} inherits its decay properties from the instantaneous projector P , as can be seen from the real-space diagrams Fig. 1. Therefore, it describes the transport of the marker from a site to the sites with which it is most strongly correlated. In Appendix D we elaborate the explicit form of the non-local marker’s currents.

The evolution of the Streda based marker C_S is determined by local continuity equation Eq. (14). Thus at the central cite its value cannot change, see Fig. 6c. As we can see, the on-site behaviour of the two markers is very different.

5 Slow markers’ dynamics

In an inhomogeneous system, the spatial distribution of the topological regions can have a decisive effect on the material’s properties. Indeed, the ability to control and modify the local topological properties – and thus the position of the zero modes on the boundaries of topological regions – would prove useful for a wide number of applications, such as dissipationless lines and new generations of electronic devices^{3-5,32}. In order to effectively control such properties in systems undergoing dynamics, one must also be able to monitor these topological characteristics through the use of a local marker. Here we consider a simple example of a problem of this kind. That is, observing the slow transformation of a finite topological domain embedded in a larger topologically trivial system. Let us describe in more detail the protocol under investigation.

Temporal Protocol — Let us consider the slow movement of a topological region inside an otherwise trivial sample as presented in Fig. 7. After a time τ , the domain with “topological” parameters shifts by one site to the right under a linear ramp. The topological phase in the model Eq. (15) is controlled by the parameter m at each site, as dictated by Eq. (16). In our case $m_1 = -3$ and $m_2 = -1$ were chosen for the trivial and topological phases respectively. Initially, the system is prepared in the ground state of $H(0)$. For the domain to move, we change the parameter m at the right boundary of the domain from m_1 to m_2 .

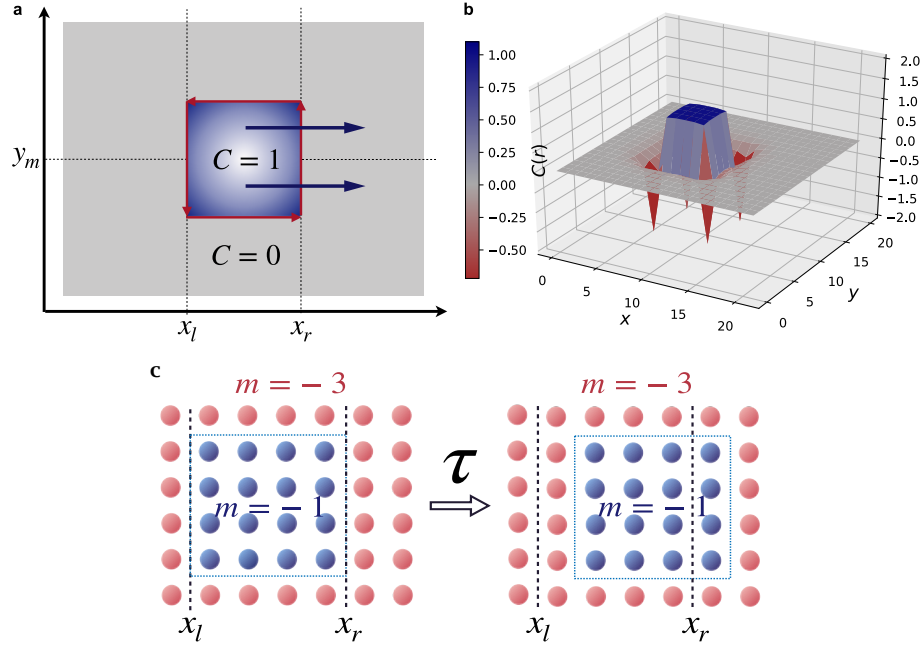


Figure 7. Scheme of the setting. **a** The domain with “Chern number” $C = 1$ (blue in figure) is drifting inside a topologically trivial sample (grey $C = 0$). The dark blue arrows indicate the drift direction of the topologically non-trivial domain. **b** The initial distribution of the LCM. **c** The evolution of the characteristic parameter m , controlling the phase in the QWZ model (15).

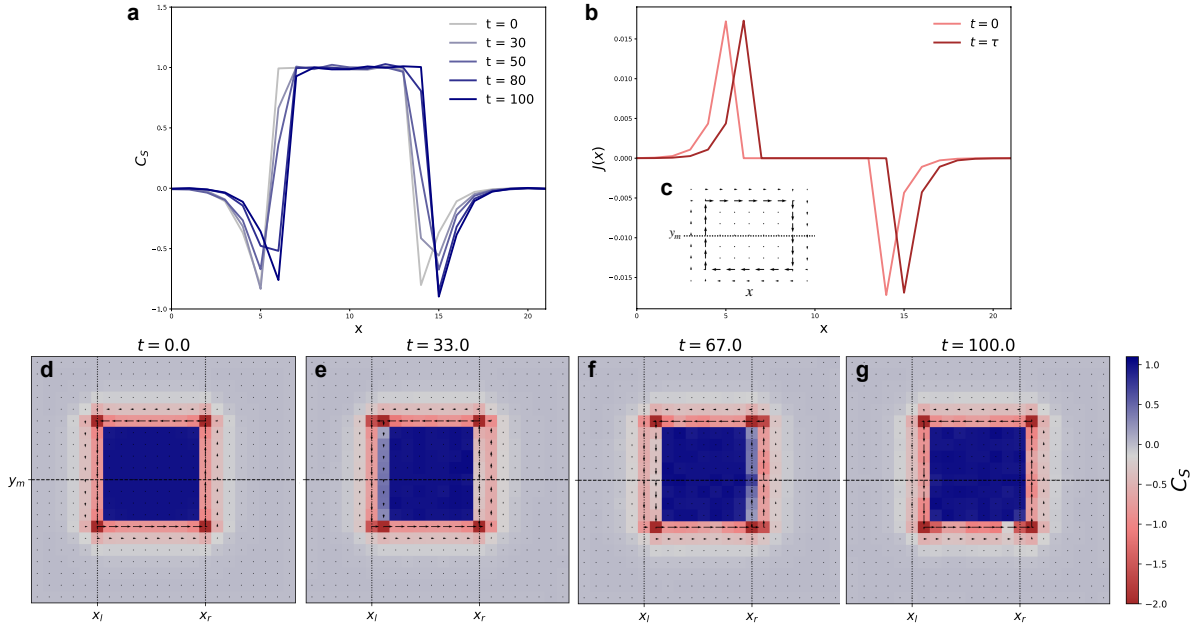


Figure 8. The movement of the “topological” domain inside the Chern insulator in the trivial phase. **a** The evolution of LCM (5) corresponding to one-site shift of the area in the slice indicated in **c**. **b** Corresponding evolution of y component of electric current in units of $et_h a/\hbar$. The current was obtained after shifting of chemical potential by 0.1Δ . **d-g** The spatial distribution of the markers and their currents on the lattice at different times. $\tau = 100 \hbar/t_h$. Lattice size is 22×21 , topological domain size is 10 by 10.

Thus, $m(x, t)$ may be parametrised as follows

$$m(x, t) = \begin{cases} m_1, & \text{for } x < x_l + [t/\tau] \\ m_2(1 - t/\tau) + m_1 \cdot t/\tau, & \text{for } x = x_l + [t/\tau] \\ m_2, & \text{for } x_l + [t/\tau] < x < x_r + [t/\tau] \\ m_1(1 - t/\tau) + m_2 \cdot t/\tau, & \text{for } x = x_r + [t/\tau] \\ m_1, & \text{for } x > x_r + [t/\tau], \end{cases} \quad (21)$$

where x_l, x_r denote the two sites on the left and right border at the beginning of time protocol respectively (see Fig. 7) and τ determines the period of protocol over which the domain shifts by one site.

Numerical results — Does a shift in the parameter’s distribution mean a real shift of the topological domain? To address this question, we calculate the electric currents generated by shifting the position of the chemical potential of the system by $\sim 0.1\Delta$. The amplitude of the electric currents in the y-direction in the middle of the sample and the distribution of currents on the bonds of the lattice is presented in Fig. 8 b-c. The shift of edge currents confirms that the topological domain has moved one site to the right.

As the system evolves, the distribution of the marker changes. The distribution of the local Chern marker follows the shift of the topological area, provided that the transformation is sufficiently slow. Fig. 8 a demonstrates how the distribution evolves over a timescale $\tau = 100$. In this regime, the distribution resembles that of the equilibrium ground state transferred as a whole one site to the right.

Local currents of the marker were observed near the borders of the topological domain. These currents are shown by the arrows in Fig. 8 d-g. The border plays the role of the charge reservoir for the bulk in the presence of a small magnetic field.

6 Discussion

Let us summarize the main results. We have demonstrated that out-of-equilibrium topological markers are highly non-local objects, due to a very large contribution from long-ranged diagrams presented in Fig. 1 to the markers’ value. Surprisingly, the long-range character of the correlations allows us to approximate the dynamics with a local continuity equation. We have found that the approximate local continuity equation works well for all the times in large translationally invariant patches. In such systems evolution always starts at the boundaries between the patches and then penetrates the bulk with the Lieb-Robinson velocity²⁹.

We have found that the markers are able to evolve in the bulk at the very early times in a large patch with a broken translation symmetry. We observe it in a quench dynamics of disordered systems in Appendix C. Remarkably, even a seemingly formal breaking of the translational symmetry, as in Hofstadter-Harper model treated in the symmetric gauge is enough to change the character of the evolution. In this case the local continuity equation approximates dynamics of the marker at late times only, when the correlations are spread across the sample.

The local continuity approximation allows us to connect the local Chern marker and on-site magnetic field induced charge in systems containing large translationally invariant patches. In such systems the local Streda marker can be used to estimate local Chern marker values. The experimental recipe is to prepare a system in two ground states: one with a small uniform magnetic field and another without. Then both samples should undergo the same evolution, during which the densities should be compared. Let us stress the dynamical Streda marker guaranties to provide topological information about the system only when it is connected with the local Chern marker. Our numerical result hints that the connection between the local Chern marker and the magnetic field response should hold more generally than we have proved analytically. One might attempt to prove the equivalence of the markers when averaged over space and time. This might allow to obtain analytical results for disordered and many-band systems.

The setting we have studied may be realized in experiment. The local Streda marker in an inhomogeneous magic-angle twisted-bilayer graphene has been studied in³⁹. The technique is based on precisely measuring the magnetization using a SQUID, while varying the filling in the system. We expect that this technology can be effectively used to read the value of the Streda response in a system undergoing dynamics. Also, modern cold atom and photonic platforms have the technologies to create and control topological interfaces^{40–42} in a single device. For a Streda marker, the dynamics of the marker can be traced by the density measurements only.

Out of equilibrium, the local Chern marker depends on the elements of the single-particle density matrix at very large distances, as we have demonstrated. These are much harder to measure in practice⁴³. At equilibrium in a system with a synthetic dimensions the local Chern marker was recently reconstructed directly⁴⁴. Hopefully, it might be possible to track its evolution as well.

Let us suggest possible extensions of our work. Interacting Chern insulators – in particular, fractional Chern insulators – provide a very interesting context in which to apply a Streda-based Chern marker. Its equations of motion can be applied to many-body systems as they do not rely on single-particle projectors. In an interacting system, the projector onto the filled states is not defined, complicating the generalization of such local markers⁴⁵. On the other hand, recent equilibrium calculations indicate that the Streda-based formula may be used as a local marker for fractional phases⁴⁶. Another important task is to find an optimal method for controlling the distribution of topological properties. This requires further analytical and numerical studies of non-homogeneous topological systems out of equilibrium.

References

1. Halperin, B. I. Quantized Hall conductance, current-carrying edge states, and the existence of extended states in a two-dimensional disordered potential. *Phys. Rev. B* **25**, 2185 (1982).
2. Teo, J. C. & Kane, C. L. Topological defects and gapless modes in insulators and superconductors. *Phys. Rev. B* **82**, 115120 (2010).
3. Büttiker, M. Absence of backscattering in the quantum Hall effect in multiprobe conductors. *Phys. Rev. B* **38**, 9375 (1988).
4. Philip, T. M. & Gilbert, M. J. High-performance nanoscale topological energy transduction. *Sci. reports* **7**, 1–10 (2017).
5. Gilbert, M. J. Topological electronics. *Commun. Phys.* **4**, 1–12 (2021).
6. Qi, X.-L. & Zhang, S.-C. Topological insulators and superconductors. *Rev. Mod. Phys.* **83**, 1057 (2011).
7. Thouless, D. J., Kohmoto, M., Nightingale, M. P. & den Nijs, M. Quantized Hall conductance in a two-dimensional periodic potential. *Phys. review letters* **49**, 405 (1982).
8. Kitaev, A. Anyons in an exactly solved model and beyond. *Annals Phys.* **321**, 2–111 (2006).
9. Bianco, R. & Resta, R. Mapping topological order in coordinate space. *Phys. Rev. B* **84**, 241106 (2011).
10. Loring, T. A. & Hastings, M. B. Disordered topological insulators via C^* -algebras. *EPL (Europhysics Lett.)* **92**, 67004 (2011).
11. Bianco, R. & Resta, R. Orbital magnetization as a local property. *Phys. review letters* **110**, 087202 (2013).
12. Bianco, R. *Chern invariant and orbital magnetization as local quantities* (Università degli studi di Trieste, 2014).
13. d’Ornellas, P., Barnett, R. & Lee, D. K. K. Quantized bulk conductivity as a local Chern marker. *Phys. Rev. B* **106**, 155124, DOI: [10.1103/PhysRevB.106.155124](https://doi.org/10.1103/PhysRevB.106.155124) (2022).
14. Irsigler, B., Zheng, J.-H. & Hofstetter, W. Microscopic characteristics and tomography scheme of the local Chern marker. *Phys. Rev. A* **100**, 023610 (2019).
15. Hastings, M. B. & Koma, T. Spectral gap and exponential decay of correlations. *Commun. mathematical physics* **265**, 781–804 (2006).
16. D’Alessio, L. & Rigol, M. Dynamical preparation of Floquet Chern insulators. *Nat. communications* **6**, 1–8 (2015).
17. Privitera, L. & Santoro, G. E. Quantum annealing and nonequilibrium dynamics of Floquet Chern insulators. *Phys. Rev. B* **93**, 241406 (2016).
18. Toniolo, D. Time-dependent topological systems: A study of the Bott index. *Phys. Rev. B* **98**, 235425 (2018).
19. Caio, M. D., Möller, G., Cooper, N. R. & Bhaseen, M. Topological marker currents in Chern insulators. *Nat. Phys.* **15**, 257–261 (2019).
20. Caio, M., Cooper, N. R. & Bhaseen, M. Quantum quenches in Chern insulators. *Phys. review letters* **115**, 236403 (2015).
21. Streda, P. Theory of quantised Hall conductivity in two dimensions. *J. Phys. C: Solid State Phys.* **15**, L717 (1982).
22. Umucalilar, R., Zhai, H. & Oktel, M. Trapped fermi gases in rotating optical lattices: Realization and detection of the topological hofstadter insulator. *Phys. review letters* **100**, 070402 (2008).
23. Golovanova, D. B., Yavorsky, A. R., Markov, A. A. & Rubtsov, A. N. Truly local topological dynamics of driven defects in Chern insulator. *arXiv preprint arXiv:2112.13574* (2021).
24. Altland, A. & Zirnbauer, M. R. Nonstandard symmetry classes in mesoscopic normal-superconducting hybrid structures. *Phys. Rev. B* **55**, 1142 (1997).
25. Benzi, M., Boito, P. & Razouk, N. Decay properties of spectral projectors with applications to electronic structure. *SIAM review* **55**, 3–64 (2013).
26. Prodan, E., Hughes, T. L. & Bernevig, B. A. Entanglement spectrum of a disordered topological Chern insulator. *Phys. review letters* **105**, 115501 (2010).
27. Bellissard, J., van Elst, A. & Schulz-Baldes, H. The noncommutative geometry of the quantum hall effect. *J. Math. Phys.* **35**, 5373–5451 (1994).
28. Mitchell, N. P., Nash, L. M., Hexner, D., Turner, A. M. & Irvine, W. T. Amorphous topological insulators constructed from random point sets. *Nat. Phys.* **14**, 380–385 (2018).

29. Lieb, E. H. & Robinson, D. W. The finite group velocity of quantum spin systems. In *Statistical mechanics*, 425–431 (Springer, 1972).
30. Harper, P. G. Single band motion of conduction electrons in a uniform magnetic field. *Proc. Phys. Soc. Sect. A* **68**, 874 (1955).
31. Hofstadter, D. R. Energy levels and wave functions of bloch electrons in rational and irrational magnetic fields. *Phys. review B* **14**, 2239 (1976).
32. Qi, X.-L., Wu, Y.-S. & Zhang, S.-C. Topological quantization of the spin Hall effect in two-dimensional paramagnetic semiconductors. *Phys. Rev. B* **74**, 085308 (2006).
33. Bernevig, B. A. Topological insulators and topological superconductors. In *Topological Insulators and Topological Superconductors* (Princeton university press, 2013).
34. Calabrese, P. & Cardy, J. Evolution of entanglement entropy in one-dimensional systems. *J. Stat. Mech. Theory Exp.* **2005**, P04010 (2005).
35. Satija, I. I. Butterfly in the quantum world. *Phys. Rev* **97**, 869–83 (2016).
36. Azbel, M. Y. Energy spectrum of a conduction electron in a magnetic field. *Sov. Phys. JETP-USSR* **19**, 634–645 (1964).
37. Peierls, R. Zur theorie des diamagnetismus von leitungselektronen. *Zeitschrift für Physik* **80**, 763–791 (1933).
38. Yilmaz, F. & Oktel, M. Ö. Artificial magnetic-field quenches in synthetic dimensions. *Phys. Rev. A* **97**, 023612 (2018).
39. Grover, S. *et al.* Chern mosaic and berry-curvature magnetism in magic-angle graphene. *Nat. Phys.* **18**, 885–892 (2022).
40. Goldman, N. *et al.* Creating topological interfaces and detecting chiral edge modes in a two-dimensional optical lattice. *Phys. Rev. A* **94**, 043611 (2016).
41. Shalaev, M. I., Desnavi, S., Walasik, W. & Litchinitser, N. M. Reconfigurable topological photonic crystal. *New J. Phys.* **20**, 023040 (2018).
42. Song, Z., Liu, H., Huang, N. & Wang, Z. Electrically tunable robust edge states in graphene-based topological photonic crystal slabs. *J. Phys. D: Appl. Phys.* **51**, 095108 (2018).
43. Ardila, L. A. P., Heyl, M. & Eckardt, A. Measuring the single-particle density matrix for fermions and hard-core bosons in an optical lattice. *Phys. review letters* **121**, 260401 (2018).
44. Chalopin, T. *et al.* Probing chiral edge dynamics and bulk topology of a synthetic Hall system. *Nat. Phys.* **16**, 1017–1021 (2020).
45. Markov, A. & Rubtsov, A. Local marker for interacting topological insulators. *Phys. Rev. B* **104**, L081105 (2021).
46. Wang, B., Dong, X.-Y. & Eckardt, A. Measurable signatures of bosonic fractional Chern insulator states and their fractional excitations in a quantum-gas microscope. *arXiv preprint arXiv:2111.01110* (2021).

7 Acknowledgements

We thank Peru d’Ornellas for many insightful discussions and in particular for sharing the details of the work¹³. Also, Peru d’Ornellas carefully read, commented and helped to edit the manuscript. Useful comments from Oleg Dubinkin are gratefully acknowledged. We thank N.Cooper and J. Bhaseen for interesting correspondence and detailed explanations of the points made in Ref.¹⁹. This work was carried out in the framework of the Russian Quantum Technologies Roadmap. A.A.M. was also also supported by the “Basis” foundation under Grant No. 18-3-01

8 Author contributions statement

D.B.G., A.R.Y. and A.A.M performed the numerical simulations. A.A.M. initiated and directed the project. Eq. 11 is due to A.N.R. All the authors contributed to the results analysis and writing the manuscript.

9 Competing Interests

The authors declare that they have no competing financial interests.

10 Code availability

<https://aryavorskiy.github.io/LatticeModels.jl/dev/>

11 Correspondence

Correspondence to A.A.Markov markov.anton92@gmail.com

A Local Streda Marker in Equilibrium

The connection between the local Chern marker and local Streda formula have been noticed in Ref¹¹. It was made on basis of the Maxwell relations and connected the averages of local Chern marker and local Streda formula over large areas in thermal equilibrium. The elaborated version of the argument can be found in Ref¹². However, this does not guarantee the local equivalence of the two quantities. In fact even in the presence of a weak diagonal disorder LCM and local Streda marker are not equivalent to each other. This is shown in Fig. 9(a). There the LCM and local Streda marker were calculated numerically for the QWZ model Eq. (15) in the presence of a gaussian disorder in on-site magnetization m . When a randomness introduced in the hopping elements, the difference becomes more apparent, see Fig. 9(b).

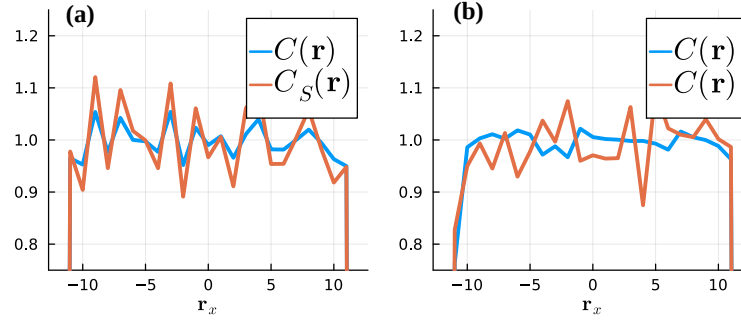


Figure 9. Topological markers in the presence of disorder The local Chern marker $C(\mathbf{r})$ (2) and on-site Streda response $C_S(\mathbf{r})$ (3) in the middle section in disordered QWZ model. **a** Weak gaussian disorder with the mean value $\Delta m = 0.1$ is added to the on-site magnetization m in the QWZ model Eq. (15). **b** Weak gaussian disorder with the mean value $\Delta t_h = 0.1$ is added to the hoppings in the QWZ model Eq. (15).

However, for two-band systems we will prove the equivalence of the Chern markers in two limits. Namely, the equivalence holds in the narrow band limit and in the particle-hole symmetric systems. In fact, we shall need more out of equilibrium. Dynamics of the LCM is determined by the non-diagonal elements of the Chern marker operator. While the local Streda marker requires the knowledge of the first-order corrections to the projectors to the filled states. Therefore we should prove Eq. (4). In the presence of a magnetic field hopping matrices between a pair of sites modifies according to the Pierls substitution³⁷:

$$H(\mathbf{r}_1, \mathbf{r}_2) = H(\mathbf{r}_1, \mathbf{r}_2) \cdot e^{i\frac{2\pi}{\phi_0} \int_{\mathbf{r}_1}^{\mathbf{r}_2} \mathbf{A}(\mathbf{r}) \cdot d\mathbf{r}}, \quad (22)$$

where $\mathbf{A}(\mathbf{r})$ is vector potential. We chose symmetric gauge $\mathbf{A}(\mathbf{r}) = \frac{1}{2} \mathbf{B} \times \mathbf{r}$. For a vanishingly small uniform magnetic field Eq. 22 can be Teylor expanded to the first order in flux $\phi = B * a^2$ through a unit cell of area a^2 . We set flux quantum $\phi_0 = 1$, a is set to one as well. The first order correction to the Hamiltonian is given by:

$$\hat{H}_B = i\pi\phi(\hat{X}\hat{H}\hat{Y} - \hat{Y}\hat{H}\hat{X}), \quad (23)$$

First order corrections to projectors \hat{P} to the filled states can be obtained from the standard perturbation theory:

$$\frac{\delta\hat{P}}{\delta\phi} = \sum_{n \in occ., m} \frac{|m\rangle\langle m|\hat{H}_B|n\rangle\langle n|}{\epsilon_n - \epsilon_m} + h.c. = \sum_{n, m} \frac{|m\rangle\langle m|\hat{Q}\hat{H}_B\hat{P}|n\rangle\langle n|}{\epsilon_n - \epsilon_m} + h.c. \quad (24)$$

Here \hat{Q} is projector to the empty states: $\hat{Q} = \mathbb{1} - \hat{P}$ and ϵ are the eigenvalues of the unperturbed hamiltonian \hat{H} . In the second equality we used the fact that corrections to a state $|n\rangle$ below the Fermi level proportional to a vector corresponding to a filled state $|m\rangle$ gets canceled out by the hermitian conjugate term in Eq. (24)

$$\sum_{n, m \in occ.} \frac{|m\rangle\langle m|\hat{P}\hat{H}_B\hat{P}|n\rangle\langle n|}{\epsilon_n - \epsilon_m} + \sum_{n, m \in occ.} \frac{|m\rangle\langle m|\hat{P}\hat{H}_B\hat{P}|n\rangle\langle n|}{\epsilon_m - \epsilon_n} = 0. \quad (25)$$

We can concentrate in consideration on the extended bulk states only. In the equilibrium this can be readily seen. The total change in density in the bulk is proportional to CN^2 , when a probe field applied. That cannot possibly be attributed to the edge states. The number of edge states electrons is proportional to N . Therefore, one might expect corrections of order of $1/N$ to the total change in bulk density in the presence of magnetic field. In dynamic we consider the effect of the edge states in the next section.

Consider the case of a two narrow bulk band. The bulk Hamiltonian might be approximated by a flat hamiltonian:

$$\hat{H}^f = \hat{P}\varepsilon_1 + \hat{Q}\varepsilon_2 = \mathbb{1}\varepsilon_2 - \hat{P}\Delta \implies \hat{H}_B^f = -i\pi\phi\Delta(\hat{X}\hat{P}\hat{Y} - \hat{Y}\hat{P}\hat{X}). \quad (26)$$

Here $\Delta = \varepsilon_2 - \varepsilon_1$ and we have used $\hat{Q} = \mathbb{1} - \hat{P}$. Substituting the expression for \hat{H}_B into Eq. (24), we obtain desired result:

$$\frac{\delta\hat{P}}{\delta\phi} = \sum_{n,m} \frac{|m\rangle\langle m|\hat{Q}\hat{H}_B^f\hat{P}|n\rangle\langle n|}{\varepsilon_n - \varepsilon_m} + h.c. = i\pi \sum_{n,m} \frac{|m\rangle\langle m|\hat{Q}\Delta(\hat{X}\hat{P}\hat{Y} - \hat{Y}\hat{P}\hat{X})\hat{P}|n\rangle\langle n|}{\Delta} + h.c. = i\pi (\hat{Q}\hat{X}\hat{P}\hat{Y}\hat{P} + \hat{P}\hat{X}\hat{P}\hat{Y}\hat{Q}) + h.c. \quad (27)$$

Let us move to the case of a symmetric w.r.t. to Fermi level spectrum, e.g. in a system with particle-hole symmetry. We require further that we consider a large enough transitionally-invariant patch, so that the bulk eigenstates may be well approximated by k states. Then, the bulk Hamiltonian might be approximated by

$$\hat{H}^s = \sum_{\mathbf{k}} \hat{H}^s(\mathbf{k}) = \sum_{\mathbf{k}} (-\hat{P}(\mathbf{k})\varepsilon(\mathbf{k}) + \hat{Q}\varepsilon(\mathbf{k})) = \mathbb{1}\varepsilon(\mathbf{k}) - 2\hat{P}(\mathbf{k})\varepsilon(\mathbf{k}) \implies \hat{H}_B^s = -i \sum_{\mathbf{k}} \frac{2\pi\varepsilon(\mathbf{k})\phi}{\phi_0} (\hat{X}\hat{P}(\mathbf{k})\hat{Y} - \hat{Y}\hat{P}(\mathbf{k})\hat{X}). \quad (28)$$

Substituting the result to Eq. (24) we get the same expression as before:

$$\frac{\delta\hat{P}}{\delta\phi} = \sum_{n,m} \frac{|m\rangle\langle m|\hat{Q}\hat{H}_B^s\hat{P}|n\rangle\langle n|}{\varepsilon_n - \varepsilon_m} + h.c. = i2\pi \sum_{\mathbf{k}} \frac{|m\rangle\langle m|\hat{Q}\varepsilon(\mathbf{k})(\hat{X}\hat{P}\hat{Y} - \hat{Y}\hat{P}\hat{X})\hat{P}|n\rangle\langle n|}{2\varepsilon(\mathbf{k})} + h.c. = i\pi (\hat{Q}\hat{X}\hat{P}\hat{Y}\hat{P} + \hat{P}\hat{X}\hat{P}\hat{Y}\hat{Q}) + h.c. \quad (29)$$

Therefore in both limits we considered we obtain the result from the main text:

$$\frac{\delta\hat{P}}{\delta\phi} = -2\pi i \hat{P}\hat{X}\hat{P}\hat{Y}\hat{P} + \pi i (\hat{X}\hat{P}\hat{Y}\hat{P} + \hat{P}\hat{X}\hat{P}\hat{Y}) + h.c. \quad (30)$$

The first term in equal to the \hat{C} . The other ones do not contribute to the Streda marker in equilibrium:

$$\begin{aligned} C_S(\mathbf{r}) &= \text{Tr} \left(\hat{\delta}_{\mathbf{r}} \frac{\delta\hat{P}}{\delta\phi} \right) = \text{Tr} \left(\hat{\delta}_{\mathbf{r}} \hat{C} \right) + \pi i \text{Tr} \left(\hat{\delta}_{\mathbf{r}} [\hat{X}\hat{P}\hat{Y}\hat{P} + \hat{P}\hat{X}\hat{P}\hat{Y} - \hat{Y}\hat{P}\hat{X}\hat{P} - \hat{P}\hat{Y}\hat{P}\hat{X}] \right) = \\ &= \text{Tr} \left(\hat{\delta}_{\mathbf{r}} \hat{C} \right) + \pi i \text{Tr} \left(\hat{\delta}_{\mathbf{r}} [\hat{X}\hat{P}\hat{Y}\hat{P} + \hat{P}\hat{X}\hat{P}\hat{Y} - \hat{P}\hat{X}\hat{P}\hat{Y} - \hat{X}\hat{P}\hat{Y}\hat{P}] \right) = \text{Tr} \left(\hat{\delta}_{\mathbf{r}} \hat{C} \right) = C(\mathbf{r}). \end{aligned} \quad (31)$$

Here we have used the cyclicity of trace and the fact that the $\hat{\delta}_{\mathbf{r}}$ and the position operator commute.

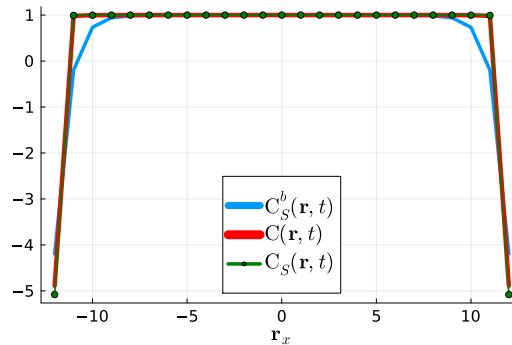


Figure 10. Bulk and edge contributions. Comparison of the bulk and edge contributions to local Streda marker $C_S(\mathbf{r})$ and LCM $C(\mathbf{r})$. $C_S^b(\mathbf{r})$ includes only the contribution from the bulk extended states, see Eq. (33). The edge states are defined as the states with the probability $p > 0.8$ to be found on the border.

In Fig. 10 $C(\mathbf{r})$ and $C_S(\mathbf{r})$ are presented for a finite sample of the QWZ model Eq. (15) in a topological phase. The derivative with respect to ϕ in the definition of $C_S(\mathbf{r})$ Eq. (3) is taken numerically. Also we calculated the response $C_S^b(\mathbf{r})$ corresponding

to the bulk extended modes only. That is we separated bulk and edge states in the projector to the filled states $\hat{P} = \hat{P}_e + \hat{P}_b$. The edge states are defined as the states $|\psi\rangle\langle\psi|$ with the probability $p > 0.8$ to be found at the edge of the sample:

$$p = \sum_{\mathbf{r} \in \text{edge}} \text{Tr}(\delta_{\mathbf{r}} |\psi\rangle\langle\psi|) > 0.8 \quad (32)$$

$C_S^b(\mathbf{r})$ is calculated using the projector to the filled bulk states only:

$$C_S^b(\mathbf{r}) = \text{Tr} \left(\hat{\delta}_{\mathbf{r}} \frac{\delta \hat{P}_b}{\delta \phi} \right) \quad (33)$$

We can see that mostly the response is determined by the bulk extended states. The difference is visible only close to the edges. Also we can see that $C(\mathbf{r})$ is almost on top of the $C_S(\mathbf{r})$.

In fact Eq. (4) includes also at least approximately the effect of scattering of filled edge states to empty edge states. Without the loss of generality let us consider the boundary in y -direction at the position $x = x_0$. When one can approximately assume that, the edge states reside only at the edge sites with $x = x_0$. Therefore they have a definite the eigenstates of \hat{X} operator. In this approximation the magnetic term in the Hamiltonian might be approximated by the commutator $i x_0 \pi \phi [\hat{H}, \hat{Y}]$. Therefore one obtains:

$$\frac{\delta \hat{P}_e}{\delta \phi} = i \pi x_0 \sum_{n,m} \frac{|m\rangle\langle m| \hat{Q} [\hat{H}, \hat{Y}] \hat{P} |n\rangle\langle n|}{\varepsilon_n - \varepsilon_m} + h.c. = i \pi x_0 (\hat{P} \hat{Y} \hat{Q} - \hat{Q} \hat{Y} \hat{P}). \quad (34)$$

Which is equivalent to Eq. (4) in an approximation that $\hat{X} = x_0(1)$, when acting on the edge states.

B Local Streda Marker out of Equilibrium

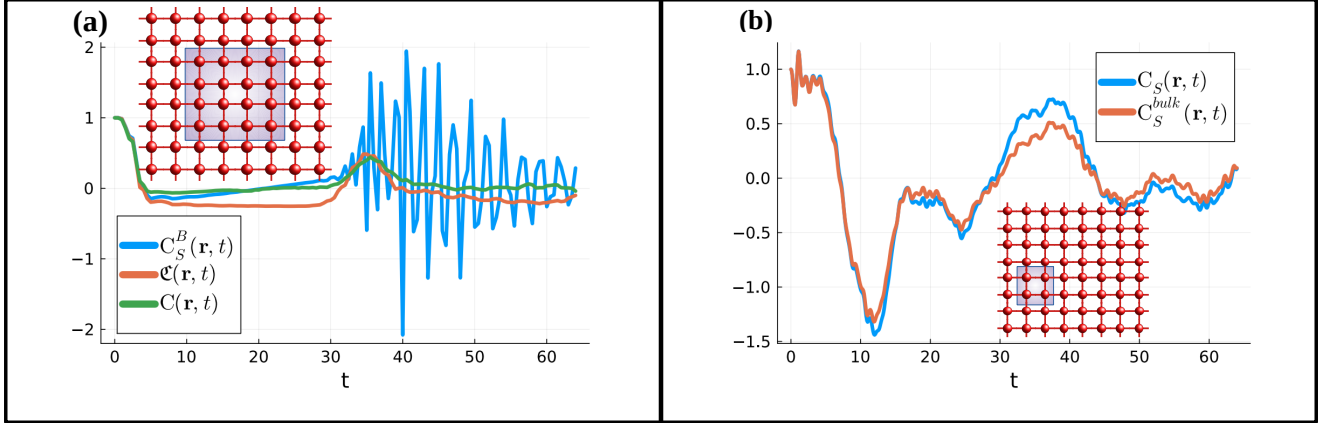


Figure 11. Local Streda Marker. (a) The average of $\mathfrak{C}(\mathbf{r}, t)$, $C(\mathbf{r}, t)$ and $C_S(\mathbf{r}, t)$ 13 over the bulk sites of 32×32 sample of QWZ model Eq. (15) in topological phase $m = -1$. $C_S^B(\mathbf{r}, t)$ corresponds to numerically taken derivative $\delta_{\psi} n(\mathbf{r})$ with a vanishingly small uniform magnetic field included in the post-quench Hamiltonian. (b) Comparison of the bulk and edge contributions to $C_S(\mathbf{r}, t)$. $C_S^{bulk}(\mathbf{r}, t)$ includes only the contribution from the bulk extended states. The edge states are defined as the states with the probability $p > 0.8$ to be found on the border. $C_S(\mathbf{r}, t)$ is averaged over a 5×5 square region with the left bottom corner at the site $(-10, -5)$.

Let us consider now the out of equilibrium on-site response to the uniform magnetic field with a flux $\phi \ll 1$. Consider the Von Neumann equations with a general time-dependent Hamiltonian $H(t)$ for the projectors $P(t) = P_0(t) + \phi \frac{\delta P(t)}{\delta \phi}$ in the presence of the small perturbation $\phi H_B(t)$, caused by the applied magnetic field:

$$i \dot{P}(t) = [\hat{H}(t) + \phi H_B(t), P(t)] = [P_0(t), H_0(t)] + \phi [P_0(t), H_B(t)] + \phi \left[\frac{\delta \hat{P}(t)}{\delta \phi}, H(t) \right] + O(\phi^2). \quad (35)$$

Therefore, the first order corrections to the on-site density in magnetic flux ϕ are coming from two sources. First source is the evolution of zeroth order projectors $P_0(t)$ governed by the perturbation $H_B(t)$. Second, they are coming from the evolution of the first-order corrections governed by the unperturbed Hamiltonian $H(t)$. Let us separate the total variation of the projector on two parts, corresponding to these two sources:

$$\frac{\delta \hat{P}(t)}{\delta \phi} = \frac{\delta \hat{P}^1(t)}{\delta \phi} + \frac{\delta \hat{P}^B(t)}{\delta \phi} = \hat{U}(t) \hat{C} \hat{U}^\dagger(t) + \hat{U}(t) [\hat{X} \hat{P} \hat{Y} \hat{P} + \hat{P} \hat{X} \hat{P} \hat{Y}] \hat{U}^\dagger(t) + \frac{\delta \hat{P}^B(t)}{\delta B}. \quad (36)$$

The term $\frac{\delta \hat{P}^1(t)}{\delta \phi}$ corresponds to the evolution of the first-order corrections to the initial state, given by Eq. (4) governed by the unperturbed Hamiltonian $H(t)$. The second part $\frac{\delta \hat{P}^B(t)}{\delta \phi}$ is obtained from the evolution in the external magnetic field. When magnetic field is included in the evolution hamiltonian time-dependent local on-site response deviates greatly from the local Chern marker at the times of order $t \approx \frac{2N}{v_{LR}}$. This is demonstrated in Fig. 11 (a). In the figure $C^B(\mathbf{r}, t)$ includes both $\frac{\delta \hat{P}^1(t)}{\delta \phi}$ and $\frac{\delta \hat{P}^B(t)}{\delta \phi}$. We can see that in late times $C^B(\mathbf{r}, t)$ averaged over the bulk sites deviates hugely from the local Chern marker.

The bulk states give the main contribution the time dependent local Streda marker, as Fig. 11 (b) indicates. There the bulk and edge states contributions to $C_S(\mathbf{r}, t)$ averaged over a 5×5 square region is presented.

C The Effect of Disorder on the Dynamics

The simplest way to destroy translation invariance and thus avoid the conditions allowing to conclude that the marker can not change in the bulk is to add disorder to the translationally invariant system. Here we discuss the effects of the weak gaussian disorder with the mean value $\Delta m = 0.1$, added to the on-site magnetization m in the QWZ model Eq. (15) to the dynamics of the markers. We consider the same quench protocol in QWZ model as before.

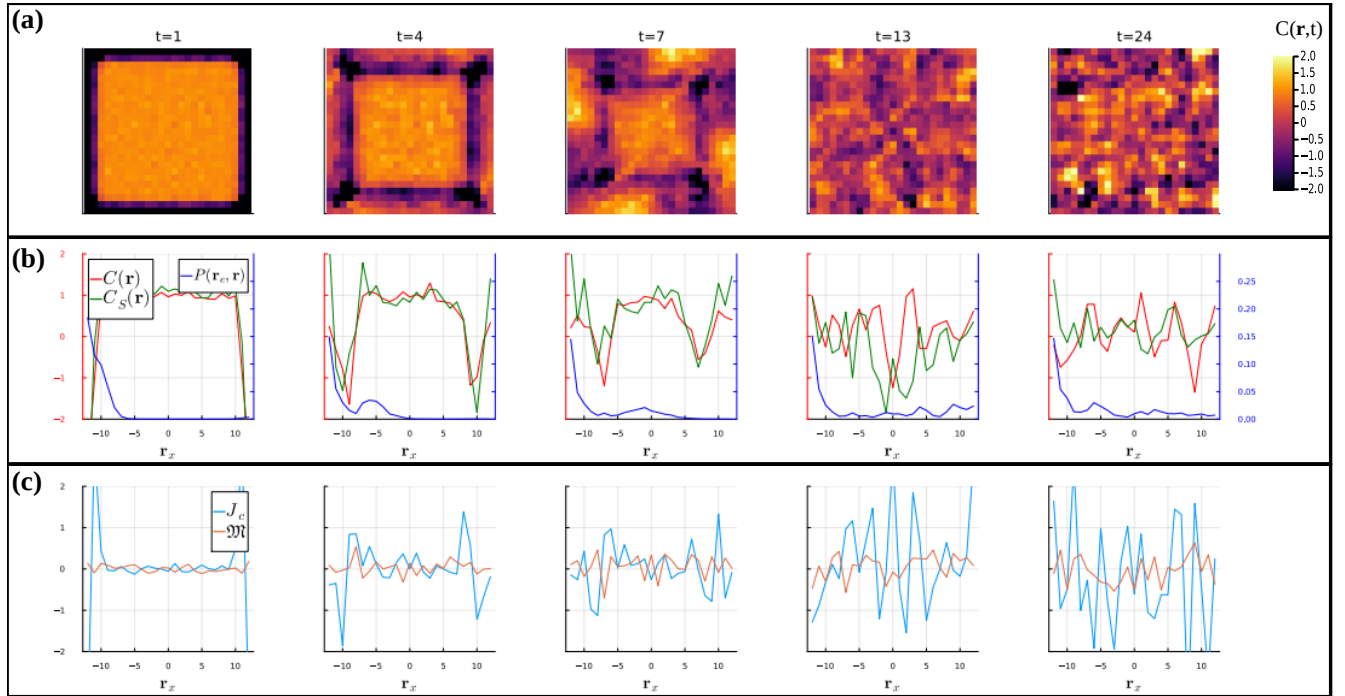


Figure 12. Propagation of different quantities in a disordered QWZ model. Weak gaussian disorder with the mean value $\Delta m = 0.1$ is added to the on-site magnetization m in the QWZ model Eq. (15). **(a)** Distribution of the local Chern marker over a 25×25 sample at different times. **(b)** Distribution of the LCM $C(\mathbf{r}, t)$, $C_S(\mathbf{r}, t)$ and the norm of matrix elements $|P(\mathbf{r}_0, \mathbf{r})|$ along the middle $-y = 0$ slice of the system. The site r_0 is chosen on the left edge. Right (blue) y-axis is for the projector matrix elements $|P(\mathbf{r}_0, \mathbf{r})|$; Left (red) y-axis is for markers' distributions. **(c)** Distributions of the $J_c(\mathbf{r})$ and $\mathfrak{M}(\mathbf{r})$ along the middle $-y = 0$ slice of the system at different times.

How different quantities propagate in a disordered sample is presented in Fig. 12. We can see that the currents of the marker are non-zero in the bulk from the very start of evolution. Therefore, it comes as a no surprise that \mathfrak{M} terms now are more

significant when it was in the translation-invariant case. This can be seen in Fig. 13b. However, at later times as long-range correlations are built, J_c gives the dominant contribution. The scaling of the ratio J_c/\mathfrak{M} keeps its linear form with the system size, as we can see from Fig. 13d. There the square root of their spectral powers ratio is presented as in the main text Eq. (18) averaged over 50 realisations of disorder.

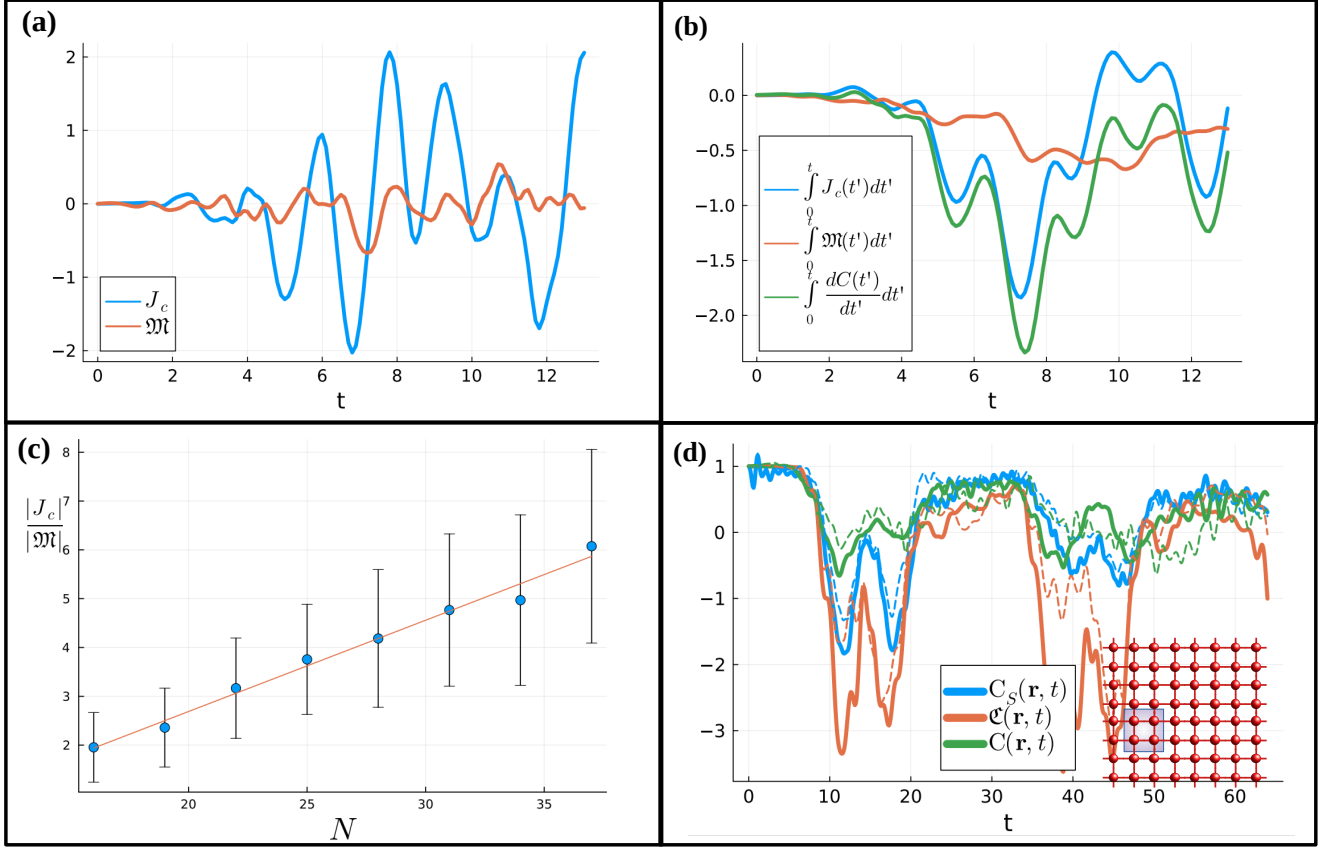


Figure 13. Quench dynamics in a disordered QWZ. Weak gaussian disorder with the mean value $\Delta m = 0.1$ is added to the on-site magnetization m in the QWZ model Eq. (15). **(a)** Time evolution of $J_c(\mathbf{r}_b)$ and $\mathfrak{M}(\mathbf{r}_b)$ at a fixed site $\mathbf{r}_b = (-7, -6)$ in the bulk of a 25×25 sample. **(b)** Time evolution of the LCM $C(\mathbf{r}_b, t)$ at \mathbf{r}_b and integral contribution to $C(\mathbf{r}_b, t)$ from $J_c(\mathbf{r}_b, t)$ and $\mathfrak{M}(\mathbf{r}_b, t)$ **(c)** Square root of the spectral power F (see the main text Eq. (18)) of ratio of the time-dependencies $J_c(\mathbf{r}_b, t)$ and $\mathfrak{M}(\mathbf{r}_b, t)$ as a function of the system's size N averaged over 50 realization of the disorder. **(d)** Time dependencies $C_S(\mathbf{r}_b, t)$, $C(\mathbf{r}_b, t)$ and $\mathfrak{C}(\mathbf{r}_b, t)$ averaged over a 4×4 square region with the left bottom coordinate at a fixed site $\mathbf{r}_b = (-7, -6)$ on a 25×25 sample. Solid lines correspond to a translationally invariant system, the dashed ones to the disordered case.

D \mathfrak{M} currents

The \mathfrak{M} terms are responsible for the teleportation of the marker to the sites correlated to a given one. Therefore they describe non-local currents Here we discuss a way to reasonably define them.

Local electric currents

Consider a non-interacting lattice system with a generic tight-binding hamiltonian:

$$\hat{H} = \sum_{\mathbf{r}_1, \mathbf{r}_2} H^{ss'}(\mathbf{r}_1, \mathbf{r}_2) \hat{c}_s^\dagger(\mathbf{r}_1) \hat{c}_{s'}(\mathbf{r}_2) + h.c., \quad (37)$$

here the index s stands for on-site degrees of freedom, e.g. spin and orbital.

For a physical quantity local in operators $\hat{c}_s^\dagger(\mathbf{r})$ and $\hat{c}_s(\mathbf{r})$ the locality of dynamics follow from the equations of motion. Consider for example the electron density. The Heisenberg equation for the density operator $\hat{\rho}(\mathbf{r}) = \sum_s \hat{c}_s^\dagger(\mathbf{r}) \hat{c}_s(\mathbf{r})$ reads:

$$\dot{\hat{\rho}}(\mathbf{r}) = i[\hat{H}, \hat{\rho}(\mathbf{r})] = -i \sum_{\mathbf{r}_1, s, s'} H^{ss'}(\mathbf{r}, \mathbf{r}_1) \hat{c}_s^\dagger(\mathbf{r}) \hat{c}_{s'}(\mathbf{r}_1) + h.c. \quad (38)$$

Naturally, one interprets the right hand side as a flow of the electrons from the site \mathbf{r} to other sites \mathbf{r}_1 . This leads us to the definition of bond currents:

$$\hat{j}^b(\mathbf{r}, \mathbf{r}') = -i \sum_{s, s'} H^{ss'}(\mathbf{r}, \mathbf{r}') \hat{c}_s^\dagger(\mathbf{r}) \hat{c}_{s'}(\mathbf{r}') + h.c. \quad (39)$$

Non-local currents of LCM

The situation with the LCM is different as formally it contains *all* the operators $\hat{c}_s^\dagger(\mathbf{r})$. Let us concentrate on the \mathfrak{M} terms only, slightly changing notation as compared to the main text.

$$\mathfrak{M}(\mathbf{r}) = -2\pi i \varepsilon^{\alpha\beta} \sum_s \left(\langle \mathbf{r}_s | \left[\hat{P} \hat{J}^\alpha \hat{P}, \hat{P} \hat{R}^\beta \hat{P} \right] | \mathbf{r}_s \rangle \right) \quad (40)$$

Here $\varepsilon^{\alpha\beta}$ is the Levi-Civita symbol. This term could not be localized to the neighborhood sites as was shown in Section 4.3. Therefore the best one can hope that it can be cast to a form of quasi-local currents, so that the following conditions holds:

- Non-local continuity equation: $\dot{C}(\mathbf{r}, t) = \sum_{\mathbf{r}'} \mathfrak{J}(\mathbf{r}, \mathbf{r}')$, here summation runs over all sites of the system
- Skew-symmetry: $\mathfrak{J}(\mathbf{r}, \mathbf{r}') = -\mathfrak{J}(\mathbf{r}', \mathbf{r})$
- $\mathfrak{J}(\mathbf{r}, \mathbf{r}')$ decay is controlled by \hat{P} .
- Invariant under a change of coordinates: $\hat{\mathbf{R}}' = \hat{\mathbf{I}}\mathbf{R}_0 + \hat{\mathbf{R}}$. Note that under translation $\hat{P} \hat{R}'^\alpha \hat{P} = \hat{P} \hat{R}^\alpha \hat{P} + \hat{P} R_0^\alpha$

Currents \mathfrak{J} satisfying these properties are no unique. For example, let us present a possible form of a translationally invariant expression:

$$\begin{aligned} \mathfrak{M}(\mathbf{r}) &= -2\pi i \varepsilon^{\alpha\beta} \sum_s \left(\langle \mathbf{r}_s | \hat{P} \hat{J}^\alpha \hat{P} \hat{R}^\beta \hat{P} - \hat{P} \hat{R}^\beta \hat{P} \hat{J}^\alpha \hat{P} + \hat{P} \hat{J}^\alpha \hat{P} \hat{R}^\beta \hat{P} - \hat{P} \hat{J}^\alpha \hat{P} \hat{R}^\beta \hat{P} | \mathbf{r}_s \rangle \right) = \\ &= -2\pi i \varepsilon^{\alpha\beta} \sum_{s, s', \mathbf{r}'} \left(\langle \mathbf{r}_s | \hat{P} \hat{J}^\alpha \hat{P} | \mathbf{r}'_{s'} \rangle \langle \mathbf{r}'_{s'} | \hat{P} \hat{R}^\beta \hat{P} | \mathbf{r}_s \rangle - \langle \mathbf{r}_s | \hat{P} \hat{R}^\beta \hat{P} | \mathbf{r}'_{s'} \rangle \langle \mathbf{r}'_{s'} | \hat{P} \hat{J}^\alpha \hat{P} | \mathbf{r}_s \rangle + \right. \\ &\quad \left. + \langle \mathbf{r}_s | \hat{P} | \mathbf{r}'_{s'} \rangle \langle \mathbf{r}'_{s'} | \hat{P} \hat{J}^\alpha \hat{P} \hat{R}^\beta \hat{P} | \mathbf{r}_s \rangle - \langle \mathbf{r}_s | \hat{P} \hat{J}^\alpha \hat{P} \hat{R}^\beta \hat{P} | \mathbf{r}'_{s'} \rangle \langle \mathbf{r}'_{s'} | \hat{P} | \mathbf{r}_s \rangle \right) = \sum_{\mathbf{r}'} J^{\mathfrak{M}}(\mathbf{r}, \mathbf{r}'). \end{aligned} \quad (41)$$

Here we added and subtracted terms $\langle \mathbf{r}_s | \hat{P} \hat{J}^\alpha \hat{P} \hat{R}^\beta \hat{P} | \mathbf{r}_s \rangle$ to insure the translation invariance of the currents. Also, we inserted the resolution of identity in position basis $|\mathbf{r}'_{s'}\rangle \langle \mathbf{r}'_{s'}|$ so that the currents satisfy the other requirements. The procedure is quite arbitrary and thus we can not guarantee the uniqueness of the currents.

The currents $J^{\mathfrak{M}}(\mathbf{r}, \mathbf{r}')$ are indeed very non-local as we can see from Fig. 14 a. There we calculated them numerically for the quench in QWZ model from the site $\mathbf{r}_b = (-7, -6)$ to all the others at time $t_f = 4.8$, as in the main text Section 4.1. We can see that the \mathfrak{M} causes teleportation of the markers' current to all the sites correlated to a given one.

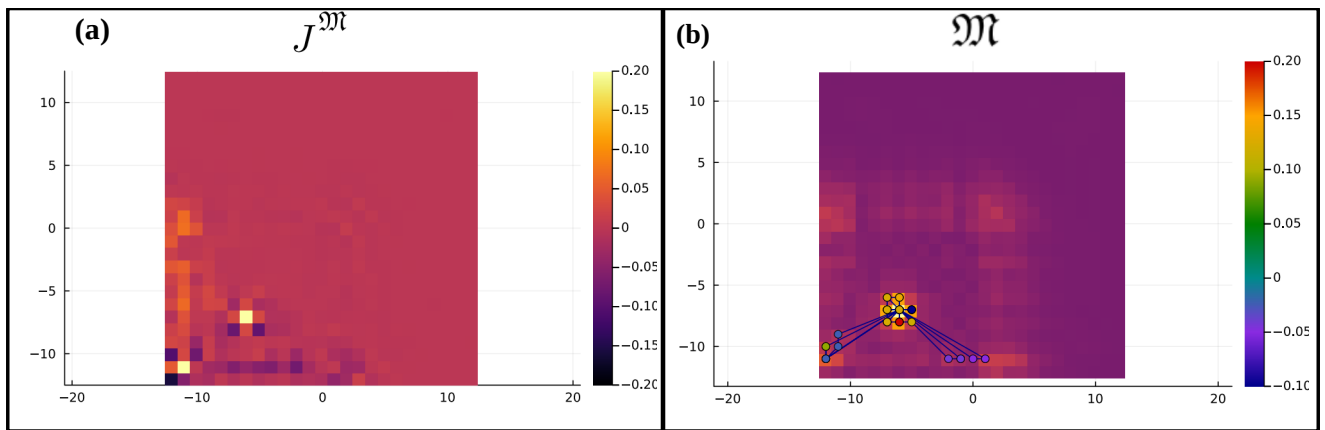


Figure 14. \mathfrak{M} currents. **(a)** Non-local currents $J^{\mathfrak{M}}(\mathbf{r}_b, \mathbf{r}')$ from the site $\mathbf{r}_b = (-7, -6)$ to all the others at time $t_f = 4.8$, as in the main text Section 4.1. **(b)** Ten the most contributing real-space diagrams as in Section 4.1 for $\mathfrak{M}(\mathbf{r}_b, t_f)$. The diagrams are plotted above the distribution $|P(\mathbf{r}_b, \mathbf{r})|$